Martian precession and rotation from Viking lander range data [1]

C. F. Yoder and E. M. Standish
Jet Propulsion Laboratory, Pasadena, California

Abstract

The spatial orientation of the Martian pole of rotation and axial rotation parameters have been determined at a midpoint in the Viking epoch (January 1, 1980). The mean obliquity ϵ and node ψ angles are $\epsilon = 25.1894° \pm 0.0001$, $\psi = 35.4796° \pm 0.0002 (2\sigma)$. The mean precession rate is $\dot{\psi}_o = -7.83 \pm 0.30$ arc sec yr^{-1}. The corresponding moment estimate is $C/MR_e^2 = 0.355 \pm 0.015$ and covers two extreme theoretical estimates. Seasonal (annual and semiannual) variations in Mars' rotation angle have also been observed and are 279 ± 100 and 311 ± 100 milliarc-second of angle (mas) respectively, after correcting for a general relativity effect. A simple model has been constructed for the main contribution involving seasonal mass exchange between the ice caps and atmosphere where the air pressure at the Viking 1 lander site is a proxy for the global ice cap/air pressure histories. The annual term is about 190 mas smaller and differs in phase by $\sim 30°$ compared to the model prediction. The semiannual term is 100 mas larger and also differs in phase by $\sim 30°$ compared to the model. A combination of tidally driven rotation changes, zonal winds, polar motion and ice cap model deficiencies may account for any discrepancy. The upcoming Pathfinder lander and Mars Global Surveyor missions carry ranging transponders which can dramatically improve our knowledge of Mars' interior through precise determination of the precession rate and detection of core and tidal effects. We advocate that plans be developed for a coordinated campaign of simultaneous ranging and Doppler tracking to each transponder.

Introduction

There has been some controversy concerning Mars' polar moment of inertia C. Theoretical estimates have been obtained using the known gravity coefficient $J_2 = (C - \frac{1}{2}(B+A))/MR_e^2$ and different philosophies to recover the hydrostatic part J_{2h} supported by rotation. Each employ the second harmonic coefficients C_{22} and S_{22} ($4\sqrt{C_{22}^2 + S_{22}^2} = 4J_{22} = (B-A)/MR_e^2$) to subtract a nonhydrostatic contribution based either on the hypothesis that Tharsis volcanic construct is the dominant source [*Reasenberg*, 1977; *Kaula*, 1979; *Kaula et al.*, 1989; *Kaula and Asimow*, 1991] of nonhydrostatic support or that hidden sources are involved [*Bills*, 1989]. Assume

$$
\begin{aligned}
C &= C_h + \Delta C \\
B &= A_h + \Delta B \\
B &= A_h + \Delta A
\end{aligned}
\tag{1}
$$

where C_h and A_h are the hydrostatic component of the polar and mean equatorial moments, respectively. The hypothesis of *Goldreich and Toomre* [1969] is that any internally supported lateral density variations caused by crustal, thermal or chemical properties orient themselves such that

$$
\Delta C \geq \Delta B \geq \Delta A.
\tag{2}
$$

One can relate J_2, J_{22} and the hydrostatic $J_{2h} = (C_h - A_h)/MR_e^2$ and eliminate the dependence on ΔA to obtain

$$
J_2 - 2J_{22} = J_{2h} + (\Delta C - \Delta B)/MR_e^2.
\tag{3}
$$

Reasenberg [1977] and *Kaula et al.* [1989] argue that the Tharsis volcanic construct is primarily responsible for the observed $B - A$ factor based on the large size of this topographic feature, the high correlation of Tharsis with the B moment and the ability to estimate the gravity contribution of this feature from the observed $B - A$ difference. Effectively they adopt $\Delta C = \Delta B$. Note that under the above assumption in Eq.(2) the resulting J_{2h} is an upper bound.

$$
J_{2h} = 0.001832
\tag{4}
$$

Given this "hydrostatic" J_{2h}, the polar moment of inertia follows from the standard formula from Clairaut

$$
C = \frac{2}{3}MR_e^2 \left(1 - \frac{2}{5}\sqrt{\frac{5m_R}{m_R + 3J_2} - 1} + O(J_2) \right)
\tag{5}
$$

and is $0.365MR_e^2$ (using $m_R = \omega^2 R^3/GM = 0.004570$). *Bills* [1989, 1990] argued that this high correlation is unjustified, that hidden sources might be as large and it might be better to assume that the moment difference $\Delta C - \Delta B = \Delta B - \Delta A$ and

$$
J_{2h} = J_2 - \frac{3}{2}J_{22}
\tag{6}
$$

The resulting polar moment recovered from (5) and (6) is $0.345MR_e^2$. The apparently small differences in moment from these two different approaches have profound implications for composition and core size. In fact, *Ohtani and Kamaya* [1992] find that such a small moment as $0.345MR_e^2$ is geochemically implausible.

Smith and Zuber [1996] have analyzed Martian spacecraft occultation data and obtain among other things a revised estimate of the mean triaxial shape of Mars. The mean figure radii found are $a = 3399.5$ km, $b = 3394.3$ km and $c = 3376.5$ km about the x, y and z axes, respectively, and the uncertainties are ~ 100 m. The alignment of this topographic ellipsoid differs by $\sim 5°$ from the axes defining the principal moments. The observed flattening is

$$
f \simeq (\frac{1}{2}(a+b) - c)/R = 0.00602
\tag{7}
$$

while the observed $(a-b)/R = 0.00154$. The hydrostatic flattening of Mars is

$$
f_h \simeq \frac{1}{2}(m + 3J_{2h}) \simeq 0.00503
\tag{8}
$$

If the same argument is applied to the flattening, then only the a axis is affected by the Tharsis construct and the hydrostatic flattening from (7) is $(b-c)/R = 0.00525$, which is close to (8). This small difference may imply either that the hydrostatic J_{2h} in (4) should be larger (say, $J_{2h} = 0.00204$) or there is an additional, perhaps crustal source to the flattening which might reduce J_{2h} .

A moment greater than $0.365MR_e^2$ seems nonphysical. However certain mechanisms might be at work here which would allow $\Delta C < \Delta B$ and still maintain its present orientation. First, the icy polar caps and any solid material they entrain primarily contribute to A and B moments but not to C. The caps will reorient themselves based on the mean yearly solar insolation even if Mars' mantle attempts to reorient because $\Delta C < \Delta B$. The second possibility is that the rotationally induced oblateness is partially frozen in place due to substantial cooling of the crust and upper mantle. Note that only 4% of J_{2h} is required to

be rigidly fixed to maintain neutral stability to polar wander if $C = 0.370$.

The primary objective here is to examine Viking range data to obtain an observational constraint on precession rate and hence moment C. We also examine other geophysical observable factors such as climate-driven seasonal variations in Mars axial rotation [*Caze- nave and Balmino*, 1981] and solar tides [*Konopliv and Yoder*, 1996]. We briefly discuss how moment constrains internal structure, how a fluid core effects short-period nutations [*Sasao et al.*, 1980; Hilton, 1992] and wobble. Complementary parameters such as the second degree potential Love number k_2 and its correlation with composition and core size are also discussed. Another motive is to promote the ranging capabilities of the upcoming Pathfinder and Mars Global Surveyor (MGS) missions. First, we shall consider a variety of geophysical models for Mars interior. These models will provide a plausible range for parameters such as moments of inertia of mantle and core and potential Love number k_2 which affect Mars orientation changes and tidal gravity field [*Hilton, 1992*].

Mars' Internal Structure

Mars' basic structure may include a fluid Fe-FeS core, an elastic mantle whose basic chemistry is dominated by oxidized forms of Mg and Fe, and a thin, less dense crust. Finer details include the possible existence of a Martian low-velocity zone (indicative of partial melt) and internal density contrasts such as the spinel transition observed at about 400-km depth on Earth [*Basaltic Volcanism Study Project*, 1981; *Ohtani and Kamaya*, 1992]. Structure profiles have been constructed using the same technique applied to Venus [*Yoder*, 1995b], where a simple Earth profile [*Dziewonski et al.*, 1975] for density, rigidity μ and bulk modulus (and expressed in terms of pressure) serves as the base state. Compositional mantle changes are characterized in terms of changes in the molar fraction χ_M (χ_M =Mg/(Mg + Fe)) of magnesium to iron from an Earth-like value of 0.89. This Earth-like profile is varied by estimating the change in a parameter such as μ with temperature T, pressure P_r and χ_M using the arithmetic mean of the Hashim-Strikman bounds [*Hashim*, 1983] for a forsterite/fayalite mixture, then determining the fractional change in this parameter with P_r (or depth), and finally, applying this to the nominal model. For example, the rigidity beneath the crust [*Kumazawa*

and Anderson, 1969; *Sumino*, 1979] used to estimate this fractional change is

$$\frac{\mu(P_r, T, \chi_M)}{\text{kbar}} = \begin{aligned} &509 + 302\chi_M \\ &+ (750 + 1050\chi_M)P_r/\text{kbar} \\ &- (75 + 55\chi_M)(T/10^3 {}^\circ\text{C}). \end{aligned} \quad (9)$$

Figure 1 presents eight models for the Martian mantle in which χ_M and temperature (as an offset from a nominal profile) are varied. Curves are shown for $\chi_M = 70$, 75, 80, and 89%. Two thermal profiles characterized by $\Delta T = \pm 200^\circ$ C with respect to that of the Earth's mantle and at the same pressure at depth are employed. This temperature offset is applied for mantle pressures greater than 30 kbar. Crustal thickness is fixed at either 100 km ($\Delta T = +200^\circ$) or 50 km ($\Delta T = -200^\circ$) to maximize its effect on moment of inertia. Each of these mantle profiles are joined at an arbitrary radius with a core whose composition (here represented by molar fraction χ_C =FeS/(Fe+FeS) is adjusted to match the known total mass. We presume that a plausible range is $0 < \chi_C < 1$ although geochemically the expected range is much smaller [i.e., *Laul*, 1986; *Schubert and Spohn*, 1990; *Schubert et al.*, 1992]. The resulting total moment of inertia, core moment and χ_C are displayed in Figures 2 and 3.

Figure 4 shows potential Love number k_2 versus total moment. The k_2 Love number is correlated with core composition (see Figure 5). However, the correlation of k_2 and vertical displacement Love number h_2 with core radius is even stronger as shown in Figure 6.

Core density and composition can also be inferred from these parameters if a reasonable model for crustal thickness can be inferred from topography-gravity field correlations or from direct measurement using a seismic network. Finally, measurement of the core ellipticity e_c from its influence on the seasonal nutations could provide a significant constraint on Martian mantle convection if it differs from its hydrostatic value [*Yoder*, 1995b].

Nutation Model and Results

The precession and nutation of a planet due to the gravitational torque provided by the Sun are described by the formulas

$$\begin{aligned} \psi &= \psi_0 + \dot\psi_0 (t - t_\circ) - \delta\psi \\ \epsilon &= \epsilon_0 + \dot\epsilon_0 (t - t_\circ) + \delta\epsilon \end{aligned} \quad (10)$$

3

where ϵ_0 and ψ_0 are epoch obliquity and nodal longitude, respectively (see Figure 7) while and $\delta\epsilon$ and $\delta\psi$ are periodic components [*Smart*, 1953; *Plummer*, 1960; *Lyttleton et al.*, 1979; *Borderies*, 1980; *Groten et al.*, 1996]. In the case of Earth nutation models [e.g., *Smart*, 1953], the pole longitude is measured from the vernal equinox to a fixed point on the ecliptic. This accounts for the minus sign for the longitude variation in (10), since we have adopted Lyttleton et al. nutation model.

The secular precession rates are

$$
\begin{aligned}
\dot{\psi}_0 &= \quad \dot{\psi}_0^* \, \delta_C \left[\cos I - \sin I \cot \epsilon \cos(\psi - \Omega) \right] \\
\dot{\epsilon}_0 &= - \quad \dot{\psi}_0^* \, \delta_C \sin I \sin(\psi - \Omega) \\
\delta_C &= \quad 0.365 M R_e^2 / C
\end{aligned}
\tag{11}
$$

The factor

$$
\begin{aligned}
\dot{\psi}_0^* &= \quad -\frac{3}{2} \frac{J_2}{0.365} \frac{n^2}{\omega} \frac{\cos \bar{\epsilon}}{(1 - e^2)^{3/2}} \\
&= \quad -7.6064 \pm 0.0004'' \mathrm{yr}^{-1}
\end{aligned}
\tag{12}
$$

is well determined, and the uncertainty is entirely due to the J_2 gravity coefficient [*Smith et al.*, 1993; *Konopliv and Sjogren*, 1995] (also see Table 1). The mutual inclination or obliquity $\bar{\epsilon}$ to orbit is

$$
\cos \bar{\epsilon} = \cos I \cos \epsilon + \sin I \sin \epsilon \cos(\Omega - \psi). \tag{13}
$$

The secular obliquity rate $\dot{\epsilon}_0$ vanishes to first order if one chooses the orbit of Mars at a reference epoch t_o (here t_o = January 1, 1980) as the reference orbit such that $I(t = t_o) = 0$. Therefore any nonzero $\dot{\epsilon}_0$ rate is purely geometrical to first order.

In addition, the precessional motion is sometimes referred to a precessing reference frame defined by the mean orbital nodal rate $\dot{\Omega}$ ($\dot{\Omega} = -0.000180°/\mathrm{d}$ is a six year average, and is adopted in DE403 [*Standish et al.*, 1995]). The relationships between the moving solid body angles referenced to the stationary frame fixed at time t_0 and the moving (overbarred) frame are

$$
\begin{aligned}
\dot{\psi}_0 &= \quad \dot{\bar{\psi}}_0 + \dot{\Omega} \cos I \\
\dot{\epsilon}_0 &= \quad \dot{\bar{\epsilon}}_0 + \dot{\Omega} \sin I \sin \overline{\psi}_0(t_0) \\
\dot{\phi} &= \quad \dot{\bar{\phi}} - \dot{\Omega} \sin I \cos \overline{\psi}_0(t_0)
\end{aligned}
\tag{14}
$$

Six years of Viking lander range data are a small though highly accurate subset of the astrometric data defining the planetary ephemeris DE403/LE403 [*Standish et al.*, 1995]. There are 1282 normal points obtained during about 200 range passes, and the reduced data have RMS residuals of 2-3 m during any

one day and about 7-12 m overall. The difference is due to a combination of solar plasma effects and calibration errors. The range signature ρ to a lander is related to the orbit and orientation of Mars' figure by

$$
\begin{aligned}
\rho &\simeq \quad d - \mathbf{R} \cdot \widehat{\mathbf{d}} \\
\mathbf{R} \cdot \widehat{\mathbf{d}} &= \quad R_z \sin \delta_d + R_\perp \cos \delta_d \cos H_d
\end{aligned}
\tag{15}
$$

where the component involving the Earth-based radar network is ignored. The cylindrical lander coordinates are R_{zi}, $R_{\perp i} = \sqrt{R_{xi}^2 + R_{yi}^2}$ and longitude λ_i of the ith lander. The remaining variables depend on the Mars' longitude L, and longitude L_d and hour angle H_d relative to Earth.

$$
\begin{aligned}
\sin \delta_d &\simeq \quad \sin \epsilon \sin(L_d - \psi) \\
H_d &\simeq \quad \phi + \psi + \lambda_i - L_d \\
L_d &= \quad L + \arcsin((r_\oplus/d)\sin S) \\
d &= \quad \sqrt{r^2 + r_\oplus^2 - 2 r r_\oplus \cos S} \\
\cos S &= \quad \widehat{\mathbf{r}} \cdot \widehat{\mathbf{r}}_\oplus
\end{aligned}
\tag{16}
$$

Separation of the various components primarily involves detection of the different temporal frequency dependences of the various components. There were two Viking landers, and contemporaneous ranges to the two sites can isolate the part dependent on the R_z component of the lander location. The fast component involving the Martian rotation angle ϕ is the easiest part to isolate; however, its sensitivity to the obliquity and node are reduced. Nutations and precession happen to preserve $\omega_3 = \dot{\phi} + \dot{\psi} \cos \bar{\epsilon}$. Therefore the sensitivity to the obliquity and node tends to come through the $\cos \delta_d$ modulation of the hour angle factor in (15). The relative sensitivity of the off-axis and z components of $\mathbf{R} \cdot \widehat{\mathbf{d}}$ to obliquity is $\sim 1/2 \sin \epsilon R_\perp / R_z$.

Several solutions with different model solution parameters and data subsets have been examined to determine a plausible uncertainty for both the orientation of Mars at an epoch near the middle of the Viking mission (January 1.0, 1980, or JD 2444239.5) and the spin rate and precession rate. The first column in Table 2 shows a solution which includes all data and solves for 184 parameters, including a seasonal model for Mars rotation. This model includes four parameters which absorb annual and semiannual variations in axial rotation of Mars.

$$
\begin{aligned}
\phi &= \quad 252.3003° + \dot{\phi} \, t + C1 \cos L^* + \\
&\qquad C2 \cos 2L^* + S1 \sin L^* + S2 \sin 2L^*
\end{aligned}
\tag{17}
$$

The angle argument L^* rate is the Martian sidereal year and the phase of L^* is zero at the chosen epoch (here January 1, 1980).

The remaining five solutions consider subsets of the parameters and data in order to access realistic error bounds. Column 2 removes the seasonal model, and this change leads to $\sim 2\sigma$ changes in epoch obliquity, longitude ψ, and rates $\dot\psi$ and $\dot\phi$. Columns 3-6 fit just the Viking lander range points and limit the solution parameters to 47 or less, of which six constrain the orbit of Mars. Columns 4-6 omit Mars' orbit from the solution. Column 5 also omits the obliquity rate while column 6 omits the seasonal model. The correlation matrix shown in Table 3 corresponds to a 15-parameter solution set specific to Mars rotation. The Viking data set is remarkably effective in separating the parameters, except for strong correlations of the spin rate and node rate and the 1980 epoch spin longitude and Lander 1 longitude. These two rates $\dot\psi$ and $\dot\phi$ are highly anticorrelated such that their sum is almost unchanged. Therefore, the sensitivity to these rates comes from the term in (15) proportional to $R_\perp$. This interpretation is supported by the fact that $\sigma(R_z) \sim 6\sigma(R_\perp)$ (see Table 4 for lander coordinates).

Comparison of columns 1 and 3 (which differ primarily in the data set) show 2σ changes in obliquity and the semidiurnal coefficient $S2$. Although the Viking data provide the dominant constraint on Mars' orientation, there are Mars' radar ranging closure points and Mariner 9 spacecraft ranging that both compete with the Viking data in constraining the orbit of Mars. There are also two very long baseline interferometry (VLBI) positions of the Phobos spacecraft at Mars that help fix its plane-of-sky position in February and March 1989. These changes in rotation parameters demonstrate the correlation of Mars' orbit parameters, particularly the orbit inclination and node with some of the parameters defining the figure orientation of Mars.

The observed secular obliquity rate should be zero. Since the observed rate is about 3 times the formal sigma, we should consider that the formal error in other parameters must be expanded by some factor perhaps as large as 3. The uncertainty in the obliquity and projected node angle $\psi_0 \sin\epsilon_0$ at the epoch are both about 180 mas or 3 m at Mars' surface. An examination of these solutions indicates that the mean obliquity is less stable than the projected node. A conservative estimate of the node $\psi_0 \sin\epsilon_0$ uncertainty during the Viking epoch is ~ 300 mas or about 5 m and could be reduced if estimates of the seasonal terms and Mars orbit parameters are improved. Ranging to Pathfinder lander in 1997 should result in a pole determination at least as good

as that from Viking. The change in pole position is $\dot\psi_0 \sin\epsilon_0 \Delta t \sim 55$ arc sec over this period, and therefore the accuracy of the inferred precession rate should be improved to $\leq 1\%$.

The solutions for the precession rate in columns 1 and 2 (Table 2) are clearly extremes, and the validity of either depends on the plausibility of the seasonal terms. The standard deviations for these parameters are an order of magnitude smaller than those associated with analysis of the orbits of Phobos and Deimos (see Table 5) for precession of Mars' equator. We demonstrate in the next section that the observed seasonal coefficients can plausibly be explained in terms of the ice cap and air pressure variations. Still, we believe that the most reliable estimate for the precession rate is a mean of these six solutions with augmented uncertainty:

$$\dot\psi_o = -7.83 \pm 0.30 \text{ arc sec yr}^{-1} \qquad (18)$$

Another reason is that the precession rate solutions from data restricted to the Viking ranges are less sensitive to the seasonal terms and tend toward this median value. The corresponding moment estimate is

$$C/M R_e^2 = 0.355 \pm 0.015 \qquad (19)$$

and is between the two extremes discussed earlier. In general, this value tends to favor the hot interior models over the cold models and Mg over Mg+Fe molar fraction $\chi_M > 80\%$.

Seasonal Changes in Mars' Rotation

The Viking data reveal that there are seasonal changes in rotation [*Reasenberg et al.*, 1980] which are probably due to surface climate. The observed change in rotation rate from Viking data analysis (column 1 in Table 2) is

$$\delta\phi = -[432 \sin(\ell - 22°8) + 318 \sin(2\ell + 35°1)] \text{ mas} \qquad (20)$$

when expressed in terms of the orbital mean anomaly ℓ (the argument $\ell = 151.16°$ on January 1, 1980). The realistic uncertainty in each amplitude is about 100 mas (2σ) and 15° in phase from a comparison of the four solutions for the seasonal coefficients (columns 1, 3, 4, and 5 in Table 2). Also, the analysis assumed that each data point is independent. A more pessimistic (and realistic) assumption is that data obtained during a pass are correlated (i.e., are biased).

5

This interpretation increases errors by about a factor of 2. The seasonal solution results in a significant reduction of the Viking RMS residuals of about 11%.

The above signature in (20) includes a variation due to general relativity and planetary motion. Clocks on Mars (hence Mars rotation) run slow by a factor $(1 - GM_\odot/c^2 r - \frac{1}{2}v^2/c^2)$ [Sears and Brehme, 1968] relative to standard time. The periodic variations in Mars rotation due to the variation in orbit radius r is

$$\delta\phi_{\text{rel.}} = - \begin{bmatrix} 175.8\sin\ell + 8.2\sin 2\ell + \\ 0.6\sin 3\ell \end{bmatrix} \text{mas.} \quad (21)$$

If this is subtracted from (20), the remainder is

$$\delta\phi = - \begin{bmatrix} 279\sin(\ell - 37°\!.0) + \\ 311\sin(2\ell + 36°\!.0) \end{bmatrix} \text{mas} \quad (22)$$

The objective is to determine if we can account for this signature.

The seasonal change in solar flux at Mars' two poles causes the frost caps to wax and wane, absorbing from or liberating CO_2 to the atmosphere during the appropriate season. The two polar contributions have nearly opposite phases. However, the effects of different cap size, polar topography, thermal inertia, and albedo result in a ±20% variation in local air pressure at the two Viking sites. The change in mass of the north and south caps is 3.5×10^{15} kg and 8.1×10^{15} kg, respectively [Hess et al., 1979, 1980; Kieffer et al., 1992]. Cazenave and Balmino (1981) have obtained a realistic estimate of the change in Mars' rotation due to the pole to equator migration of CO_2, attempting to include the effect of finite (and variable) cap size and zonal winds. We will reconsider these contributions, guided in part by Chao and Rubincam's [1990] study.

A harmonic analysis of surface pressure P_{V1} at Viking 1 lander covering 2 Martian years [Tillman et al, 1993] results in the following expression:

$$\begin{aligned} P_{V1} = \ & [7.939 + 0.660\cos(\ell - 67°\!.2) \\ &+ 0.566\cos(2\ell + 1°\!.8) \\ &+ 0.105\cos(3\ell - 7°\!.5) \\ &+ 0.061\cos(4\ell - 11°\!.9) \\ &+ 0.014\cos(5\ell - 49°\!.4)] \text{ mbar,} \end{aligned} \quad (23)$$

when expressed in terms of mean anomaly ℓ. Pressure is a maximum at northern winter solstice which happens to occur near $\ell = 0°$ and Mars is closest to the sun. The mean pressure at the lander 1 site is high compared to the global mean 5.6 mbar [Kieffer et al., 1992] by about 30% . The pressure at the

Lander 2 site which covered 1 Martian year and was strongly affected by a dust storm, had a very similar variation. The only exception was the annual term, which is about 0.08 mbar larger at the Lander 2 site even after correcting for the greater mean pressure at Lander 2.

The predicted change in spin rate $\delta\dot\phi \equiv \delta\omega$ due to surface mass displacement or internal momentum exchange can be derived from the conserved angular momentum $C\omega$. Since total mass is conserved, the variation in moment can be related to a variation in the J_2 gravity coefficient,

$$\delta C/M R^2 = \frac{2}{3}\delta J_2. \quad (24)$$

The part due to changes in surface mass redistribution related to seasonally variable, zonally symmetric ice cap loads and air pressure field is given by [Yoder et al., 1981]

$$\begin{aligned} \delta\dot\phi \ = \ & \omega_\circ \frac{4\pi R^4}{3C_m}(1 + k'_{2m}) \\ & \int [q_{\text{ice}}(\varphi, t) + P(\varphi, t)/g] \\ & (\tfrac{3}{2}\cos^2\varphi - \tfrac{1}{2})\sin\varphi d\varphi. \end{aligned} \quad (25)$$

It is assumed that the core is fluid and decoupled from the mantle for axial variations in rotation. The second-degree load number for mantle k'_{2m} happens to satisfy $k'_{2m} \simeq -k_{2m}$ and is smaller than the whole body value because of the positive contribution to k_2 from the core.

If the atmosphere is uniformly distributed with co-latitude φ and zonal winds are weak, then rotational changes depend only on the load history $q_{\text{ice}}(\varphi, t)$ of the two ice caps. However, there is a significant second harmonic departure of Mars' surface from the geoid allowing air pressure to contribute to nonspherical gravity. Adopt a spherical harmonic expansion (basis function $Y_{nm}(\varphi, \lambda)$) of degree n and tesseral order m) of the pressure and surface topography $H(\varphi, \lambda)$ relative to the geoid:

$$\begin{aligned} P(\varphi, \lambda, t) &= \sum P_{nm}(t)Y_{nm}(\varphi, \lambda) \\ H(\varphi, \lambda) &= \sum H_{nm}Y_{nm}(\varphi, \lambda) \end{aligned} \quad (26)$$

Chao and Rubincam [1990] estimate that the topographic component of the coefficient $P_{nm}(t)$ is related to the mean pressure $\overline{P}(t)$ by

$$P_{nm}(t) \simeq -2\overline{P}(t)H_{nm}/Z \quad (27)$$

if the atmospheric scale height $Z \simeq 11$ km is large compared to the overall topography and is indepen-

dent of latitude. They also find that the time variation in a gravity harmonic coefficient $\delta C_{nm}^{P}(t)$ is

$$\delta C_{nm}^{P}(t) = -\frac{3}{2n+1}\frac{\overline{P}(t)}{\overline{\rho}gR}\frac{H_{nm}}{Z}. \quad (28)$$

where $\overline{\rho} = 3.933$ g/cm^3 and surface gravity $g = 3.72$ m/s^2.

Define the following coefficient K_{20}^{P},

$$K_{20}^{P} = \frac{\int P(\varphi,t)(\frac{3}{2}\cos^2\varphi - \frac{1}{2})\sin\varphi d\varphi}{\int P(\varphi,t)\sin\varphi d\varphi} \quad (29)$$
$$= -\frac{2}{5}H_{20}/Z,$$

(adopting unnormalized $Y_{nm}(\varphi,\lambda)$ in (26)). A recent topography solution [*Bills and Nerem*, 1995] finds $H_{20} = -0.76$km . Hence $K_{20}^{P} \simeq 0.028$. The ice load $q_{ice}(\varphi,t)$ is not well determined although models developed by *Pollack et al.*, [1993], which employ imaging to constrain the time history of the cap boundary, seem to account for the above pressure variation. If the two caps exactly counterbalance each other, that is as one cap sublimates a given mass, the other condenses it, then there is no change in pressure. This does not necessarily mean that there is no change in moment if the two caps extend to different latitudes in each hemisphere or have different mass distributions with latitude.

The observed change in mean air pressure $\delta\overline{P}(t) = \overline{P}(t) - \langle\overline{P}(t)\rangle$ is determined by mass conservation and is

$$2\delta\overline{P}/g = -\int(q_{ice}(\varphi,t) - \langle q_{ice}(\varphi,t)\rangle)\sin\varphi d\varphi. \quad (30)$$

The angle brackets indicate the mean value. If the ice caps are concentrated near the poles, one can use the above mean pressure to estimate the change in rotation. Furthermore, we shall adopt

$$\delta\overline{P} = \frac{\langle\overline{P}(t)\rangle}{\langle\overline{P}(t)_{V1}\rangle}\delta\overline{P}_{V1}(t) = K_{V1}\delta\overline{P}_{V1}(t). \quad (31)$$

Thus the Viking Lander 1 pressure will be a proxy for the global ice cap/atmosphere exchange.

Finally, in order to take into account the finite extent of the caps, we shall also define

$$K_{20}^{caps} = \frac{\int q_{ice}(\varphi,t)(\frac{3}{2}\cos^2\varphi - \frac{1}{2})\sin\varphi d\varphi}{\int q_{ice}(\varphi,t)\sin\varphi d\varphi} \quad (32)$$

and again K_{20}^{caps} is assumed to be independent of time. This constancy with time only holds if $q_{ice}(\varphi,t)$ factors (i.e. $q_{ice}(\varphi,t) = (Q_N(\varphi) - Q_S(\varphi))T(t)$).

From (23, 25, and 29-32), the effect of ice is therefore (1 mbar $(\omega/n\overline{\rho}gR) = 277.9$ mas)

$$\begin{aligned}\delta\phi_{caps} = \ -\overline{K}_{20}\{&367\sin(\ell - 67°2) + \\ &157\sin(2\ell + 1°7) \\ &+19\sin(3\ell - 7.5) + ..\} \text{ mas},\end{aligned} \quad (33)$$

with

$$\overline{K}_{2j} = (1 + k'_{2m})\frac{MR_e^2}{C_m}K_{V1}(K_{2j}^{caps} - K_{2j}^{P}). \quad (34)$$

The factor $(1 + k'_{2m})MR_e^2/C_m$ ranges form 2.3 to 2.8 (see Figure 9), although its most likely value is 2.5. The factor $K_{V1} \simeq 0.70$, $K_{20}^{P} \simeq 0.028$, while the cap geometry factor K_{20}^{caps} is less certain, since it is sensitive to such factors as whether the cap sublimates/accretes at its edges or more globally changes over the whole cap surface. We estimate $K_{20}^{caps} \simeq 0.745$ for uniform caps which both extend down to 55° latitude. Thus the annual term has a magnitude $\sim$470 mas for nominal values of the mantle moment and Love numbers. This prediction is about 190 mas larger in amplitude than observed (see (22)) and is about twice the $\sim$100 mas uncertainty. The annual phase difference is 31°, or about twice the estimated 15° uncertainty.

Comparison of the observed and predicted semi-annual term indicates that the predicted amplitude is this time about 110 mas smaller than observed while the phases differ by 34°. These contributions from $\delta\phi_{caps}$ and the observed annual and semiannual terms are compared in Figures 8 and 9, respectively, including some additional sources to be discussed. The model predictions for the triannual UT term are shown in Figure 10 and have a combined amplitude of less than 30 mas. Although small, the contribution from tides and ice cap changes are more nearly comparable.

Cazenave and Balmino, [1981] estimated the effect of zonal winds and found them negligible ($\leq 2 \times 10^{-10}\omega$), but this may not be correct [*Zuber et al.*, 1996]. Global mean circulation models for Mars' atmosphere' [*Haberlee et al.*, 1993] show large zonal winds which range from 5 m/s near the surface to $\sim$100 m/s at $\sim$0.01 mbar pressure. The RMS weighted wind velocity in the northern winter is $\sim$20 m/s. During northern winter, the zonal winds tend to subrotate in the southern hemisphere and super-rotate in the northern. The axial momentum balance appears to favor the southern hemisphere and, if true,

would imply that the mantle must speed up in response. This wind pattern reverses during northern summer. This suggests that the wind contribution to Mars' rotation is 180° out-of-phase with the mass part.

The mean atmospheric pressure is about 5.6 mbar, from which we deduce a mass of 2.3×10^{19} g. If mean zonal winds fluctuate globally by ± 5 m/s over a Martian year, then the change in spin is $\pm 1.4 \times 10^{-9}$ (equivalent to ~ 190 mas in $\delta\phi$) and is about $1/2$ the change due to mass redistribution.

The tidally driven variations [e.g., *Yoder et al.*, 1981] are proportional to k_{2m}/C_m, where k_{2m} is the reduced Love number of the mantle. The leading terms are

$$
\begin{aligned}
\delta\phi_{\text{tidal}} \quad = -k_{2m}\frac{MR_e^2}{C_m}[&96.6\sin\ell \\
&+62.3\sin 2(\ell + \widetilde{\omega} - \psi) \\
&+14.1\sin(3\ell + 2(\widetilde{\omega} - \psi)) \\
&+6.8\sin 2\ell \\
&-5.9\sin(\ell + 2(\widetilde{\omega} - \psi))]\text{ mas}
\end{aligned} \quad (35)
$$

The $k_{2m}MR_e^2/C_m$ factor ranges from 0.3 to 0.8 for the range of Mars' models considered (see Figure 11) although the likely value is near its lower bound. The corresponding amplitudes for the annual term range from 30 to 80 mas. The annual tidal contribution when added to the ice cap component in (33) tends to slightly improve the agreement with the Viking solution.

Clearly, we need to obtain a realistic estimate of the wind contribution and the potential time dependence of the $K_{20}^{\text{caps}}(t)$ factor before the discrepancy between models and observations can be reliably assessed. Another factor which might affect the model is mass redistribution involving wind blown-dust, but since this part tends to move east-west rather than north-south, we believe this source is small. Polar motion might also corrupt the observed signature. *Chao and Rubincam* [1990] estimate that a 1° ice cap offset from the spin axis will excite ~ 20 mas seasonal polar motion as the caps change size. Finally, errors in the adopted short-period nutation model could also corrupt the Viking observations. We shall briefly review estimates of these two contributions.

Polar Motion

Define a polar motion variable $m = m_x + im_y$ (here $m_x = \omega_x/\omega_z$, etc. and $i = \sqrt{-1}$), which is referenced to a principal axis frame. This frame is related to the adopted frame for mapping by the longitude rotation $\lambda_{P.A.} = 74.75°$. Polar motion is caused primarily by surface mass redistribution $\Psi(t) = C_{21} + iS_{21}$, and any excited free wobble is dampened by solid friction at a rate [*Lambeck*, 1980; *Yoder*, 1995a,b]

$$
\tau_W^{-1} = \omega_o k_2 m_R / Q_W (MR^2/3C \quad (36)
$$

where $m_R = \omega^2 R/g$.

The dynamical equation is

$$
\begin{aligned}
\frac{d}{dt}m - \quad &i\{\left[(e_o\omega_o + i\tau_W^{-1})\right]m \\
&+2\omega_o\exp(i\lambda_{P.A.})e_{22}m^*\} \\
&= i\omega_o\Psi(t)
\end{aligned} \quad (37)
$$

The coefficients $e_o = (J_{20} - \frac{1}{3}k_2 m_R)MR_e^2/C_m$, $e_{22} = J_{22}MR_e^2/C_m$, and m^* is a complex conjugate of m. The free wobble is

$$
\begin{aligned}
m \quad = \quad m_o\{&\exp i\sigma_W t - \frac{2e_{22}}{\sigma_W + e_o}\exp(i\lambda_{P.A.}) \\
&\exp - i\sigma_W t)\}\exp - t/\tau_W
\end{aligned} \quad (38)
$$

where $\sigma_W = \omega_o\sqrt{e_o^2 - 4e_{22}^2}$ is the wobble frequency. The factor $2e_{22}/(\sigma_W + e_o) \simeq 0.03$ and therefore the free motion is primarily prograde and almost circular. The factor k_2/Q deduced from the tidal contraction of Phobos' orbit [*Sinclair*, 1989; *Yoder* 1995a] is $1.62 \pm 0.02 \times 10^{-3}$. However, the tidal flexing period is 5.6hr and is 10^{-3} smaller than the wobble period. If the wobble quality factor $Q_W(\simeq 200d) \approx Q(5.6$ hours), then the wobble decay time is about 60 years.

The excitation function Ψ due to surface mass redistribution is

$$
\begin{aligned}
\Psi \quad = \quad -\frac{R^4}{3C_m}(1 + k_{2m}') \times \\
\int (q_{ice}(\varphi, \lambda, t) + g^{-1}P(\varphi, \lambda, t)) \times \\
3\cos\varphi\sin^2\varphi\exp i\lambda d\varphi d\lambda.
\end{aligned} \quad (39)
$$

The excitation on the right-hand side of (39) depends on the time-dependent ice cap load $q(\varphi, \lambda, t)$ and air pressure of harmonic degree 2 and tesseral order 1. The caps at greatest extent during winter are reasonably symmetric with respect to the pole and the centroid of the cap boundaries deviate by $\leq 3°$ from the geographic pole. On the other hand, the residual caps during summer are quite asymmetric with respect to the pole [*James et al.*, 1992].

As was done with rotation, introduce a (complex) constant K_{21}^P which relates the above variation in pressure to the mean pressure. Explicitly,

$$K_{21}^{\mathrm{P}} = \frac{3 \int P(\varphi, \lambda, t) \cos\varphi \sin^2\varphi d\varphi d\lambda}{\int P(\varphi, \lambda, t) \sin\varphi d\varphi d\lambda} \qquad (40)$$
$$= -\tfrac{3}{5} H_{21}/Z.$$

The height $H_{21} = (0.47 + 0.03i)$ km [*Bills and Nerem,* 1995] and $K_{21}^{\mathrm{P}} \simeq -0.026 - 0.002i$. Assume that each ice cap is offset by $\varphi_{\mathrm{o}}^{\mathrm{N,S}}$ toward longitude $\lambda_{\mathrm{o}}^{\mathrm{N,S}}$.

$$q_{\mathrm{ice}}(\varphi, \lambda, t) = (1 + \varphi_{\mathrm{o}} \cos(\lambda - \lambda_{\mathrm{o}})) q_{\mathrm{ice}}(\varphi, t) \qquad (41)$$

The above model for $q_{\mathrm{ice}}(\varphi, \lambda, t)$ could just as well be interpreted as a variation in load thickness with longitude. Define the coefficient K_{21}^{caps},

$$K_{21}^{\mathrm{caps}} = K_{21}^{\mathrm{N}} + K_{21}^{\mathrm{S}}, \qquad (42)$$

and

$$K_{21}^{\mathrm{N,S}} = \frac{\tfrac{3}{2}\varphi_{\mathrm{o}}^{\mathrm{N,S}} \exp i\lambda_{\mathrm{o}}^{\mathrm{N,S}} \int_{\mathrm{N,S}} q_{\mathrm{ice}}(\varphi, t) \cos\varphi \sin^2\varphi d\varphi}{\int q_{\mathrm{ice}}(\varphi, t) \sin\varphi d\varphi}.$$
$$(43)$$

Again, this coefficient is constant if the angle and time dependence for the ice load can be factored. Adopting $q_{\mathrm{ice}}(\varphi, t) = (Q_N(\varphi) - Q_S(\varphi))T(t))$, we find for uniform caps extending to 35° colatitude,

$$K_{21}^{\mathrm{caps}} = \frac{0.91\left(Q_{\mathrm{S}}\varphi_{\mathrm{o}}^{\mathrm{S}} \exp i\lambda_{\mathrm{o}}^{\mathrm{S}} - Q_{\mathrm{N}}\varphi_{\mathrm{o}}^{\mathrm{N}} \exp i\lambda_{\mathrm{o}}^{\mathrm{N}}\right)}{Q_{\mathrm{S}} - Q_{\mathrm{N}}}. \qquad (44)$$

The difference between K_{21}^{caps} and the rotation coefficient $K_{20}^{\mathrm{caps}} \simeq 0.75$ given similar approximations is that the above coefficient can depend on the sum of the ice loads in each hemisphere divided by the difference if $\lambda_{\mathrm{o}}^{\mathrm{N}} = \lambda_{\mathrm{o}}^{\mathrm{S}} + 180°$ and $\varphi_{\mathrm{o}}^{\mathrm{N}} = \varphi_{\mathrm{o}}^{\mathrm{S}}$. For this case $K_{21}^{\mathrm{caps}} \simeq 2.5\varphi_{\mathrm{o}}^{\mathrm{S}} \exp i\lambda_{\mathrm{o}}^{\mathrm{S}}$.

The excitation function can then be related to the mean pressure and is

$$\Psi = -\frac{\delta P(t)}{g\bar{\rho}R}\overline{K}_{21} \qquad (45)$$

where $\overline{K}_{21}$ is defined in (34). Although the factor K_{21}^{caps} is unknown, a plausible estimate of the magnitude for $\overline{K}_{21} \simeq 0.15$ (equivalent to setting $K_{21}^{\mathrm{caps}} = -2K_{21}^{\mathrm{P}}$).

Figure 13 displays the estimated mean polar motion amplitude using this estimate for Ψ. The most interesting result is that the forced motion from ice cap changes is $10 - 20$ mas at 1, 1/2, and 1/3 year before falling off at 1/4 year to 5 mas or less. This effect is entirely due to the resonance effect caused by the 193 to 212 day wobble period.

The excitation of free polar motion will depend on the line width of the 1/3 year and 1/4 year excitation. Proportionally, one of these two spectral lines is at least as close to the wobble frequency as Earth's annual forcing is to the Chandler wobble. Since Earth's mean Chandler wobble amplitude is as large as the annual forcing, the expectation should be that the wobble is about as large as either the 1/3 year or 1/4 year forced motion. Another way of estimating the free wobble is to use the spectral amplitude in the pressure near the wobble period as $\delta P_W \simeq 0.01$ mbar [*Barnes,* 1981; *Zurek et al.,* 1992]. The mean free wobble period due to this noise is

$$< m > \sim \frac{2\delta P_W}{g\bar{\rho}R}\overline{K}_{21}\sqrt{\omega_{\mathrm{o}}^2\tau_W/\nu_W} \qquad (46)$$

or ~ 10 mas if we again estimate $\overline{K}_{21} \sim 0.15$. The spectral power in the ice load history near the wobble period could be higher, and it is not implausible that the free wobble might be as large as 50 mas.

Short-Period Nutations

In addition to Mars quasi-secular precession, the Sun also drives short-period variations in Mars obliquity and node which result from a combination of the changing orientation of Mars' figure relative to the Sun and Mars' large orbital eccentricity. If Mars were rigid, then precise measurement of these factors would also provide an additional constraint on the polar moment, C. The rigid body amplitudes in table 6 have been calculated assuming $C = 0.365MR^2$ [*Borderies* 1980]. The *Lyttleton et al.* [1979] model for the short period terms has been adopted in this data analysis for which the equivalent moment is 0.374. Thus the rigid response could be larger by a factor of ~ 1.05 if $C = 0.355MR^2$, changing the amplitude of the semi-annual nutation by about ~ 30 mas.

Elasticity of Mars' mantle and the independent nutation of the fluid core introduces a correction factor $G(s_j)$, which is applied to the decomposed prograde and retrograde parts of $\delta\epsilon - i\sin\epsilon_0\delta\psi$:

$$\delta\epsilon - i\sin\epsilon_0\delta\psi = \sum_j G(s_j)a_+(s_j)\exp(is_jt + \theta_j)$$
$$+G(-s_j)a_-(s_j)\exp-(is_jt + \theta_j)$$
$$(47)$$

where s_j is positive. To first order, $G(s)$ is [*Sasao et al.,* 1980]

$$G(s) = 1 - \frac{k_2 m_R}{e_f} \frac{s}{\omega} + F \frac{s}{\sigma_c - s}$$
$$F = \frac{A_c}{A_m}(1 - \frac{m_R \tilde{\gamma}}{e_c}) \qquad (48)$$

The factors k_2 and $\tilde{\gamma}$ measure the elastic change in shape of the surface and core mantle boundaries, respectively, in response to tides. The parameter e_c is the dynamic ellipticity of the core-mantle boundary. The factor F is shown for three mantle profiles in Figure 14 and demonstrates that it is an excellent proxy for core radius.

The free core nutation frequency σ_c of the fluid core is

$$\sigma_c = -(C/C_m)(e_c - \tilde{\beta} m_R)\omega \qquad (49)$$

where $\tilde{\beta}$ is another elastic correction factor. The expected FCN period ranges from -330 to -220 day and could be near either 1/2 or 1/3 of a Martian year.

Figure 15 displays the nutation amplitudes for the prograde annual and semiannual $a_+(2L)$ and retrograde semiannual $a_-(2L)$ and triannual $a_-(3L)$ nutation amplitudes as a function of composition and core size. The effect of increasing core ellipticity by 7% for the $\chi_M = 89\%$ is also displayed and shows that it can be an important correction for the retrograde terms. The minimum RMS signal from these five lines is about 25 mas for plausible core size, but could be as large as 60 mas. *Folkner and Kahn* [1994] find that tracking of 2-3 landers for a Martian year could resolve the moment ratio F factor in (48) to about 0.01.

Future Missions

We have demonstrated that Viking range data are capable of detecting Mars precession to an accuracy of about 300 mas/yr and seasonal variations in rotation to an accuracy of about 100 mas/yr. Although interesting, the results are not precise enough to serve as useful constraints on either moment of inertia or surface climate. The remaining issue is to examine what can be achieved with planned or contemplated missions.

Improvement in the orientation of Mars was one of the scientific goals of the unsuccessful Russian Phobos lander mission, the failed Mars Observer mission [*Albee et al.*, 1992], the cancelled MESUR and European INTERMARSNET projects (both multiple landers) [*Kahn et al.*, 1996]. The major source of highly accurate astrometry during this decade will involve the future Pathfinder lander and MGS orbiter missions which will reach Mars in late 1997. Doppler and range data obtained from these spacecraft should provide a dramatic improvement in resolving Mars' orientation given that each carries an X-band transponder capable of ~ 2 m range and ~ 0.1 mm/s (for 10 sec integrations) Doppler tracking accuracy. The lander data alone should rapidly determine the pole orientation to within a few meters with a few months of data [*Edwards et al.*, 1992; *Folkner and Kahn*, 1994; *Folkner et al.*, this issue]. When combined with the Viking pole position, the precession rate between the 2 epochs should be determined to better than 1%. Pathfinder should also detect with greater certainty the seasonal rotation terms if the mission lasts well beyond its minimum 1 month lifetime. *Folkner et al.*, [this issue] find that a combination of Doppler and range data obtained on a regular basis (3 h/week) over 1 Martian year can reduce the uncertainty of the UT seasonal variations to 8 mas (1 year) 25 mas (1/2 year) and 7 mas (1/3 year). Polar motion is obtained to similar accuracy: (7 mas (1 year), 16 mas (1/2 and 1/3 year)). However, it is problematical whether the core moment in (48) can be detected with sufficient accuracy to usefully constrain core size from the lander data alone. The addition of orbiter and VLBI data may dramatically improve the prospect of detecting the core through its effect on nutations and tidal Love numbers. The timing precision of the X band transponder can be as small as 75 ps if this instrument is properly calibrated [*Edwards et al.*, 1992; *Kahn et al.*, 1996]. However, there may be other limitations such as signal to noise ratio (especially for the lander) which degrades the measurement to about 1 m under the best of circumstances. Clearly, even a modest improvement from combining Pathfinder and MGS ranging of even a factor of 2 to 4 could dramatically improve chances of detecting the core.

Differential Doppler tracking and ranging of the orbiter relative to the lander may improve the ability to detect a variety of geophysical and climate related effects directly from perturbation of the orbit [e. g., *Wu et al.*, 1995]. First, the seasonal changes in the CO_2 ice caps cause detectable changes in the zonal harmonics of the gravity field J_2, J_3, J_4, etc., from their long-term perturbation of either the node (even harmonics) or the orbital eccentricity (odd harmonics) [e.g., *Yoder et al.*, 1983; *Chao and Rubincam*, 1990]. The advantage of detection of, say, the J_2 variation from the related seasonal variation in rotation is that it is independent of zonal wind changes and

the moment of inertia. Estimates of the annual and semiannual amplitudes for the normalized coefficients are shown in Figure 16 and are to be compared with a estimate of the equivalent noise level achieved for Magellan gravity after being rescaled to account for the difference in mass and radius. The MGS spacecraft should do as well, since the Doppler tracking systems are comparable (both X band). Differential Doppler tracking may lower this noise level by a factor of 2 to 10, depending in part on the ability to avoid spacecraft orbit adjustments for long periods of time. Another important point is that the even harmonics depend on the sum of the loads in the two hemispheres while the odd harmonics depend on the difference in the hemispheric load histories [*Chao and Rubincam*, 1990]. Therefore the J_2, J_3 histories will determine the total change in mass in each cap. Comparison of seasonal UT and the J_2 history will isolate the mantle moment (hence core size) if a reasonable model for the zonal winds can be constructed. Improvement in the spacecraft orbit will also aid the MGS mapping mission done with both camera and laser altimeter. The most exciting possibility is direct mapping of the elevation changes associated the rise and fall of the ice caps. Roughly, 75 g/cm^2 and 110 g/cm^2 accumulate at north and south caps each season [*Zurek et al.*, 1992]. Porosity (i.e., snow) and geographic variations could easily lead to ice cap topography changes of 10 m or more. Accurate tracking of the orbiter relative to the lander may reduce the radial orbit uncertainty to less than 1 m, although this point has yet to be demonstrated. Earlier studies [*Folkner and Border*, 1990] indicate that the transverse position accuracy of 10 m can be reached using doubly differenced VLBI data.

The short-period radial Doppler signature for a polar orbiter is [*Konopliv and Yoder*, 1996]

$$\sim 0.036 k_2 \cos(2L_\odot - 2L_{sp}) \qquad \text{mm/sec.} \qquad (50)$$

This amounts to a radial displacement of about 5 $k_2$cm during a 20 min pass and which is phased with the Sun. Detection of k_2 may be possible but will require an order of magnitude improvement in Doppler sensitivity compared to that obtained for Magellan.

The MGS spacecraft will be placed in a nearly circular and polar orbit with orbit inclination adjusted to about 93° such that the orbital node precesses with the Sun and local time below the spacecraft is 1400 (day)/ 0200 (night) This means that the orbit inclination is particularly sensitive to the prograde annual nutation and if the spacecraft orbit maneu-

vers are avoided, then this perturbation will cause a long-term drift in orbit inclination with amplitude $\pi a_+ (2L)/\text{yr} \simeq 3$ mas/day (see Figure 15a and Table 6). Another means of determining the size of the core with greater sensitivity is to place the MGS spacecraft at the end of its nominal mission in a different "resonant" orbit, say, either the retrograde annual ($I \simeq 87°$) or prograde annual ($I \simeq 96°$) for which the core effects are 2-4 times larger.

Clearly, each of these distinct measurements will improve detailed models of Martian climate and general geophysical parameters such as moments of inertia of mantle and core and Love numbers. Finally, there is a wealth of planetary orbit information including improved detection of relativity parameters [*Reasenberg et al.*, 1979b; *Shapiro*, 1990], asteroid masses [*Williams*, 1984; *Standish and Hellings*, 1988] and frame ties [*Standish and Williams*, 1990; *Standish et al.*, 1995] which would result from such a project. The proposed experiment requires (1) implementation of instrument testing and calibration to achieve the highest possible precision, (2) extensive planning for the data campaign, and (3) allocation of antenna time.

References

Albee, A. L., R. E. Ardvison, and F. D. Palluconi, Mars Observer mission, *J. Geophys. Res.*, *97*, 7665-7680, 1992.

Barnes, J. R., Midlatitude disturbances in the atmosphere: A second Mars year, *J. Atmos. Sci.*, *38*, 225-234, 1981.

Basaltic Volcanism Study Project, *Basaltic Volcanism of the Terrestrial Planets*, 1286 pp., Pergamon, New York, 1981.

Bills, B. G., The moments of inertia of Mars, *Geophys. Res. Lett., 16*, 385-388, 1989.

Bills, B. G., Geodetic constraints on the composition of Mars, *J. Geophys. Res., 95,* 14,131-14,136, 1990.

Bills, B. G., and R. S. Nerem, A harmonic analysis of Martian topography, *J. Geophys. Res., 100,* 26,314-26,326, 1995.

Borderies, N., La rotation de Mars: theorie analytique analyse d'observation de l'experience Viking, Ph.D. Thesis, L'universite Paul Sabatier de Toulouse, 1980.

Cazenave, A., and G. Balmino, Meteorological effects on the seasonal variation of Mars rotation, *Geophys. Res. Lett., 8*, 245-248, 1981.

Chao, B. F., and D. P. Rubincam, Variations of Mars gravitational field and rotation due to seasonal CO_2 exchange, *J. Geophys. Res., 95,* 14,755-14,760, 1990.

Dziewonski, A., A. L. Hales, and E. R. Lapwood, Parametrically simple Earth models consistent with geophysical data, *Phys. Earth Planet Inter., 10,* 12, 1975.

Edwards, C. D., Jr., R. D. Kahn, W. M. Folkner and R. A. Preston, Mars planetary geodesy using earth-based observations of Mars landers, *AIAA Pap., 92-4666,* 1992.

Folkner, W. M. and J. S. Border, Orbiter-orbiter and orbiter-lander tracking using same-beam interferometry, paper AIAA 90-2906, presented at the AIAA/AAS Astrodynamics Conference, Am. Inst. Aeronaut. Astronaut., Portland, Oreg., Aug. 1990.

Folkner, W. M., and R. D. Kahn, Latest Mars rotation study results, *JPL IOM*, Jet Propul. Lab., Pasadena, Calif., July 21, 1994.

Folkner, W. M., R. D. Kahn, R. A. Preston, C. F. Yoder, E. M. Standish, J. G. Williams, C. D. Edwards, R. Hellings, M. Eubanks, and B. Bills, Mars dynamics from Earth-based tracking of the Mars Pathfinder lander, *J. Geophys. Res.*, this issue.

Goldreich, P., and A. Toomre, Some remarks on polar wandering, *J. Geophys. Res., 74*, 2555-2567, 1969.

Groten, E., S. M. Molodenski, and V. N. Zharhov, On the theory of Mars' forced nutation, *Astron. J., 111*, 1388-1399. 1996.

Haberlee, R. M., J. B. Pollack, J. R. Barnes, R. W. Zurek, C. B. Leovy, J. R. Murphy, H. Lee, and J. Schaeffer, Mars atmospheric dynamics as simulated by the NASA Ames general circulation model: The mean zonal circulation, *J. Geophys. Res., 98*, 3093-3123, 1993.

Hashim, Z., Analysis of composite solids, *J. Appl. Mech., 50*, 481-505, 1983.

Hess, S. L., J. A. Ryan, and J. E Tillman, The seasonal variation of atmospheric pressure on Mars as affected by the south polar cap, *J. Geophys. Res., 84*, 4559-4574, 1979.

Hess, S. L., J. A. Ryan, J. E. Tillman, R. M. Henry and C. B. Leovy, The annual cycle of pressure on Mars measured by Viking landers 1 and 2, *Geophys. Res. Lett., 7*, 197-200, 1980.

Hilton, J. L. The motion of Mars' pole, II, The effect of an elastic mantle and liquid core, *Astron. J., 103*, 619-637, 1992.

Jacobson, R.A., S. P. Synnott, and J. K. Campbell, The orbits of the satellites of Mars from spacecraft and earth based observations, *Astron. Astrophys., 225*, 548-554, 1989.

James, P. B., H. H. Kieffer, and D. A. Paige, The seasonal cycle of carbon dioxide on Mars, in *Mars*, edited by H. H. Kieffer, B. M. Jakosky, C. W. Snyder, and M. S. Matthews, pp. 934-968, Univ. of Ariz. Press, Tucson, 1992.

Jeanloz, R., and A. B. Thompson, Phase transitions and mantle discontinuities, *Rev. Geophysics, 21*, 51-74, 1983.

Kahn, R. D., W. F. Folkner, R. A. Preston, and C. D. Edwards Jr., Measurement of Mars rotational variations via earth-based radio tracking of Mars landers, *Adv. in Astronaut. Sci., 89*, 331-347, 1996.

Kaula, W. M., The moment of inertia of Mars, *Geophys. Res. Lett., 6*, 194-196, 1979.

Kaula, W. M., N. H. Sleep, and R. Phillips, More about the moment of inertia of Mars, *Geophys.Res. Lett., 16*, 1333-1336, 1989.

Kieffer, H. H., B. M. Jakosky, and C. W. Snyder, The planet Mars: From antiquity to the present, in *Mars*, edited by H. H. Kieffer, B. M. Jakosky, C. W. Snyder, and M. S. Matthews, pp. 1-34, Univ. of Ariz. Press, Tucson, 1992.

Konopliv, A. S., and W. L. Sjogren, The JPL Mars gravity field, Mars50c, based upon Viking and Mariner 9 Doppler tracking data, *JPL publ., 95-5*, 1995.

Konopliv, A. S. and W. L. Sjogren, Venus gravity handbook, *JPL publ., 96-2*, 1996.

Konopliv, A. S., and C. F. Yoder, Venusian k_2 tidal Love number from Magellan and PVO tracking data, *Geophys. Res. Lett., 23*, 1857-1860, 1996.

Kumazawa, M., and O. L. Anderson, Elastic moduli, pressure derivatives, and temperature derivatives of single-crystal olivine and single-crystal forsterite, *J. Geophys. Res., 74*, 5961-5972, 1969.

Lambeck, K., *The Earth's Variable Rotation*, 449 pp., Cambridge Univ. Press, New York, 1980.

Laul, J. C., The Shergotty consortium and the SNC meteorites: An overview, *Geochim. Cosmochim. Acta, 50*, 875-887, 1986.

Lyttleton, R. A., D. L. Cain, and A. S. Liu, Nutation of Mars, *JPL Publ., 79-85*, 1979.

Ohtani, E., and N. Kamaya, The geochemical model of Mars: An estimation from high pressure experiments, *Geophys. Res. Lett., 19*, 2239-2242, 1992.

Plummer, H. C., *An Introductory Treatise on Dynamical Astronomy*, 343 pp., Dover, Miniola, N. Y., 1960.

Pollack, J. B., R. M. Halberd, J. R. Murphy, J. Schaeffer, and H. Lee, Simulations of the general circulation of the Martian atmosphere, 2, Seasonal pressure variations, *J. Geophys. Res., 98*, 3125-3148, 1993.

Reasenberg, R. D., The moment of inertia and isostasy of Mars, *J. Geophys. Res., 82,* 369-375, 1977.

Reasenberg R. D., I. I. Shapiro, P. E. MacNeil, R. B. Goldstein, J. C. Breidenthal, J. P. Brenkle, D. L. Cain, T. M. Kaufman, T. A. Komarek, and A. I. Zygielbaum, Viking relativity experiment: Verification of signal retardation by solar gravity, *Astrophys. J., 234*, L219-L221, 1979.

Reasenberg, R. D., T. M. Eubanks, P. E. MacNeil, and I. I. Shapiro, Mars Rotation: Detection of seasonal rotation rate, (abstract), *Bull. Am. Astron. Soc., 12*, 721, 1980.

Sasao, T., S. Okubo, and M. Saito, Linear theory on the dynamical effects of a stratified core upon the nutational motion of the earth, in *Nutation and the Earth's Rotation*, edited by E. P. Federov, M. L. Smith, and P. L. Bender, pp. 165-183, Reidel, Dordrecht, 1980.

Sears, F. W., and R. W. Brehme, *Introduction to the Theory of Relativity*, pp. 195-202, Addison-Wesley, Reading, Mass., 1968.

Shapiro, I. I., Solar system tests of general relativity: Recent results and present plans, in *Proceedings of the Twelfth International Conference on General Relativity and Gravitation*, edited by N. Ashby, D. F. Bartlett, and W. Wyss, Cambridge, Univ, Press, New York, 1990.

Schubert, G., and T. Spohn, Thermal history of Mars and the sulfur content of its core, *J. Geophys. Res., 95*, 14,095-14,104, 1990.

Schubert, G., S. C. Soloman, D. L. Turcotte, M. J. Drake, and N. H. Sleep, Origin and thermal evolution of Mars, in *Mars*, edited by H. H. Kieffer, B. M. Jakosky, C. W. Snyder, and M. S. Matthews, pp. 147-183, Univ. of Ariz. Press, Tucson, 1992.

Sinclair, A. T., The orbits of the satellites of Mars determined from earth-based and spacecraft observations, *Astron. Astrophys., 220*, 321-328, 1989.

Smith, D. E., F. J. Lerch, R. S. Nerem, M. T. Zuber, G. B. Patel, S. K. Fricke and F. G. Lemoine, An improved gravity field for Mars: Goddard Mars model 1, *J. Geophys. Res., 98*, 20,871-20,889, 1993.

Smith, D. E., and M. T. Zuber, The shape of Mars and the topographic signature of the hemispheric dichotomy, *Science, 271,* 184-188. 1996.

Smart, W. M., *Celestial Mechanics*, Longmans, Green, Toronto, Ont., 1953.

Standish, E. M., Jr. and R. W. Hellings, Determination of the masses of Ceres, Pallas, and Vesta from their perturbations upon the orbit of Mars, *Icarus, 80,* 326-333, 1988.

Standish, E. M., Jr., and J. G. Williams, Dynamical reference frames in the planetary and Earth-Moon systems, in *Inertial Coordinate Systems on the Sky*, pp. 173-181, edited by J. H. Lieske and V. K. Abalakin, Kluwer Acad., Norwell, Mass., 1990.

Standish, E. M., X X Newhall, J. G. Williams, and W. M. Folkner, JPL planetary and lunar ephemerides, DE403/LE403, *JPL IOM 314.10-127* Jet Propul. Lab., Pasadena, Calif., May 22, 1995.

Sumino, Y., The elastic constants of Mn_2SiO_4, Fe_2SiO_4 and Co_2SiO_4 and the elastic properties of olivine group minerals at high temperature, *J. Phys. Earth, 27*, 209-238, 1979.

Tillman, J. E., N. C. Johnson, P. Guttorp, and D. B. Percival, The Martian annual atmospheric pressure cycle: Years without great dust storms, *J. Geophys. Res., 98*, 10,963-10,971, 1993.

Williams, J. G., Determining asteroid masses from perturbations on Mars, *Icarus 57*, 1-13, 1984.

Wu, X., P. L. Bender, and G. W. Rosbourgh, Probing the interior of Mercury from an orbiter plus single lander, *J. Geophys. Res., 100*, 1515-1525, 1995.

Yoder, C. F., Astrometric and geodetic properties of earth and the solar system, in *Global Earth Physics: A Handbook of Geophysical Constants, AGU Reference Shelf vol. 1*, edited by T. J. Ahrens, pp. 1-31, AGU, Washington, D. C., 1995a.

Yoder, C. F., Venus' free obliquity, *Icarus, 250*, 250-286, 1995b.

Yoder, C. F., J. G. Williams, and M. E. Parke, Tidal variations of Earth rotation, *J. Geophys. Res., 86*, 881-891, 1981.

Yoder, C. F., J. G. Williams, J. O. Dickey, B. E. Schutz, R. J. Eanes, and B. D. Tapley, Secular variation of Earth's gravitational harmonic J_2 coefficient from Lageos and nontidal acceleration of Earth rotation, *Nature, 303*, 757-762, 1983.

Zuber, M. T., D. E. Smith, and R. M. Haberlee, The effect of the atmosphere of Mars on the planet's rotation and gravity field, (abstract), *Lunar Planet. Sci., XXVII*, 1509-1510, 1996.

Zurek, R. W., J. R. Barnes, R. M. Haberlee, J. B. Pollack, J. E. Tillman, and C. B. Leovy, Dynamics of the atmosphere of Mars, in *Mars*, edited by H.

H. Kieffer, B. M. Jakosky, C. W. Snyder, and M. S. Matthews, pp. 835-933, Univ. of Ariz. Press, Tucson, 1992.

Table 1. Mars' Orbit and Low Order Gravity

Mars' Orbit[a]	Value	Rate
I	1.85061°	−0.25 arc sec /yr
Ω	49.57854°	−10.20 arc sec /yr
e	0.0931233	12×10^{-6}/yr
L	355.45332°	191.403066° /yr
l	19.41248°	191.399324° /yr

Mars' Gravity[b]	Value	
GM km^3/sec^2	42828.370 $\pm 0.026(3\sigma)$	
R_e	3394.2 km	
$J_2 \times 10^9$	195816 ± 90	
C_{22}	-54423 ± 43	
S_{22}	32067 ± 44	

Epoch is January 1, 2000. The mean orbital elements and their secular rates correspond to a 250 year average obtained from a numerical integration.

[a] *Yoder* [1995a] [b] *Konopliv and Sjogren* [1995].

Table 2. Solutions for Seasonal UT Changes ($C1$, $S1$, $C2$, and $S2$), Spin Rate $\frac{d}{dt}\phi$, Figure Orientation Angles obliquity ϵ, and Nodal Angle ψ and Their Secular Rates.

	Parameter	Solution 1	2	3	4	5	6
1	$C1$ (mas)	-339		-301	-243	-197	
	$\sigma(C1)$	±54		±47	±43	±43	
2	$S1$ (mas)	268		276	227	206	
		±54		±50	±43	±43	
3	$C2$ (mas)	122		91	119	140	
		±58		±40	±36	±36	
4	$S2$ (mas)	-294		-197	-206	-205	
		±54		±40	±40	±40	
5	$\frac{d}{dt}\phi$ (deg/day)	350.891985106	-243×10^{-9}	29×10^{-9}	-84×10^{-9}	-98×10^{-9}	-123×10^{-9}
		±0.000000138	$\pm131 \times 10^{-9}$	$\pm74 \times 10^{-9}$	$\pm57 \times 10^{-9}$	$\pm58 \times 10^{-9}$	$\pm58 \times 10^{-9}$
6	ϵ_0 (deg)	25.189351	25.189142	25.189231	25.189239	25.189116	25.189115
		±0.000052	±0.000047	±0.000041	0.000037	±0.000031	±0.000035
7	$\frac{d}{dt}\epsilon$ (mas/yr)	229	162	256	257		162
		±88	±85	±58	±45		±46
8	ψ_0 (deg)	35.479649	35.479479	35.479534	35.479582	35.479544	35.479427
		±0.000121	±0.000114	±0.000078	±0.000070	±0.000070	±0.000070
9	$\frac{d}{dt}\psi$ (mas/yr)	-7905	-7645	-7943	-7837	-7834	-7788
		±186	±175	±97	±80	±82	±80
	Moment C/MR^2	0.3513	0.3630	0.3495	0.3543	0.3544	0.3565
	$\sigma(C)$	±0.0089	±0.0083	±0.0043	±0.0038	±0.0038	±0.0038

Solution 1 shows part of the nominal solution (184 unknowns) using 40,674 observations. Solution 2 removes the seasonal model for Mars rotation. Accurate Mars data include 629 Mariner 9 ranges (σ of 35-120 m), Mars' range ($\sigma = \pm0.5$ km) deduced from Phobos spacecraft OD in 1989, four Phobos VLBI experiments (Mars RA and Dec with $\sigma = \pm10$ to ±100 mas)) and 1282 range points to the two Viking landers obtained during 6 years and obtained during ~200 ranging passes. Solutions 3-6 reduce the data set to just the 1282 Viking range points (1202 to Lander 1 and 80 to Lander 2). Solution 3 is limited to 47 "geometric" parameters, including the above variables, the Viking lander coordinates, nine Deep Space Network (DSN) station coordinates (longitude of one fixed), and six Mars' orbit parameters. Solutions 4-6 omit Mars' orbit. Solution 5 omits the obliquity rate $\frac{d}{dt}\epsilon$ while solution 6 omits the seasonal model (and which increases the rms residuals in solution 4 by 11%). The epoch is January 1, 1980 (MJD=2444239.5). The solution for spin rate in row 5 shows only the changes in the rate from the nominal solution in column 1. Errors are 1 standard deviation and mas=milliarc second. Moments of inertia are based on ψ solution rates in row 9 and (11) and (12).

Table 3. Correlation Matrix ($\times 10^4$) for the Reduced, 15 Parameter Set

	$C2$	$S1$	$S2$	$\frac{d}{dt}\phi$	ϵ_0	$\frac{d}{dt}\epsilon_0$
$C1$	-181	1258	-3629	1136	-3484	-2011
$C2$	10000	405	692	-285	-1992	-914
$S1$		10000	1599	2224	1108	283
$S2$			10000	-591	542	-53
$\frac{d}{dt}\phi$				10000	386	84
ϵ_0					10000	6187

	ψ	$\frac{d}{dt}\psi$
$C1$	-2120	-1913
$C2$	632	274
$S1$	-3792	-2432
$S2$	92	909
$\frac{d}{dt}\phi$	-7932[a]	-9706[a]
ϵ	148	79
$\frac{d}{dt}\epsilon$	833	311
ψ	10000	8153[a]

	$R_{\perp 1}$	R_{z1}	λ_1	$R_{\perp 2}$	R_{z2}	λ_2
$C1$	-2995	1595	1838	-674	1387	994
$C2$	-195	1092	-867	-733	962	584
$S1$	2150	-1797	3208	733	-425	2650
$S2$	1143	262	280	1034	-509	955
$\frac{d}{dt}\phi$	1013	-1075	8087[a]	-2265	520	5816
ϵ	5617	-7155[a]	24	1450	-3371	-503
$\frac{d}{dt}\epsilon$	-200	-1264	-473	-673	2897	-479
ψ	-1574	1140	-9761[a]	253	490	-7071[a]
$\frac{d}{dt}\psi$	-775	1016	-7963[a]	2370	-652	-5442
$R_{\perp 1}$	10000	-6954	1323	1884	-4902	876
R_{z1}		10000	-1108	-1643	4887	-141
λ_1			10000	-278	-378	7222[a]
$R_{\perp 2}$				10000	-3534	-814
R_{z2}					10000	666

[a] Correlations > 0.7.

Table 4. Viking Lander Coordinates for Solution 1 in Table 2 Which Are Consistent with (17) Defining ϕ.

Parameter	Value
$R_{\perp 1}$(m)	3136515.5 ± 1.6
R_{z1}	1284456.1 ± 10.4
λ_1	$311.7359° \pm 0.0011°$ E
$R_{\perp 2}$	2277375.6 ± 1.9
R_{z2}	2500053.4 ± 11.0
λ_2	$133.9676° \pm 0.0011°$ E

Note that longitudes are in a right-handed coordinate system. The z height solutions without the seasonal terms (solution 2 in Table 2) are 27 and 35m greater for Landers 1 and 2, respectively. Removal of the sea-

sonal terms also change the Earth's orbital eccentricity by $\delta e = -1.75 \times 10^{-11}$ (2.2σ) and Mars' semimajor axis by $\delta a/a = -1.13 \times 10^{-11}$ (1.2σ).

Table 5. Motion of the Pole from Satellite Orbits

Reference	Parameter	Rate
Sinclair [1989]		
	ϵ_0	$25.2001° \pm 0.0039°$
	$\frac{d}{dt}\epsilon$ (arc sec/yr)	1.44 ± 0.72
	ψ	$35.01° \pm 0.01°$
	$\frac{d}{dt}\psi$ (arc sec/yr)	-9.97 ± 1.8
Jacobson et al. [1989] Deimos		
	$\frac{d}{dt}\psi$ (arc sec/yr)	-7.080 ± 1.37
	$\frac{d}{dt}\epsilon$ (arc sec/yr)	1.65 ± 0.86
Phobos		
	$\frac{d}{dt}\psi$ (arc sec/yr)	-10.6 ± 2.7

Jacobson et al. [1989] and *Sinclair* [1989] determine the pole motion from Phobos and Deimos using spacecraft imaging data and ground-based astrometry. Sinclair solves for a common pole rate relative to the Laplacian plane while Jacobson finds rates for each satellite relative to Earth's equator. The epoch for both estimates is January 1, 1950. Sinclair's higher value is almost certainly due to Phobos. Jacobson *et al.*(1989) uses Earth's equator as a reference for which $\epsilon = 36.6°$ and $\psi = 46.3°$ for Deimos.

Table 6. Rigid Body Short Period Nutations Obtained Using *Borderies'* [1980] model with $C = 0.365/MR_e^2$.

Argument	$\delta\psi$	$\delta\epsilon$	a_+	a_-
$2(L - \psi)$	-1.0984	0.5168	0.4921	0.0247
$2(L - \psi) - \ell$	0.1047	-0.0493	0.0469	-0.0024
$2(L - \psi) + \ell$	-0.2399	0.1129	0.1175	0.0054
$2(L - \psi) + 2\ell$	-0.0408	0.0192	0.0183	0.0009
$2(L - \psi) + 3\ell$	-0.0061	0.0031	0.0029	0.0002
ℓ	0.6031	0.0	-0.3015	0.3015
2ℓ	0.0443	0.0	-0.0221	0.0221
3ℓ	0.0040	0.0	-0.0020	0.0020

Units are arc seconds. The J2000 phase of arguments are $L = \ell + \widetilde{\omega} = 355.45°$, $\ell = 19.41°$ and $\psi = 35.48°$. Changing the amplitude of these coefficients by a factor of 1.05 has a small effect on solution parameters in Table 2: $\delta C1 = 2.0$, $\delta S1 = 2.8$, $\delta C2 = -3.9$ and $\delta S2 = -2.1$ mas, while $\delta\frac{d}{dt}\psi = -5.1$ mas/yr.

16

Figure 1. Mantle density profiles as a function of mantle composition χ_M and temperature offsets ΔT. The models are constructed using Earth as a basis model [*Yoder*, 1996b]. The effect of temperature on mantle density is estimated using $\alpha_{\text{exp.}} \times 10^7 = 26 + (11 + 3\chi_M)(T/°\text{C } 10^3)$ [*Jeanloz and Thompson, 1983*].

Figure 2. Total moment of inertia and core composition χ_C versus core radius for eight mantle density profiles.

Figure 3. Total moment of inertia versus core moment of inertia.

Figure 4. Potential Love number k_2 versus moment C for six models.

Figure 5. Love number k_2 versus core composition χ_C.

Figure 6. Love numbers for potential k_2 and vertical displacement h_2 versus core radius for 3 "hot" models with $\Delta T = 200°\text{C}$. Linear fit is $h_2 = 1.81k_2 + 0.0085$ over the range shown.

Figure 7. Orientation of Mars' orbit and pole of rotation.

Figure 8. Comparison of observed annual signature for $\delta\phi$ (column 1 in Table 2), and an estimate from ice cap sublimation and accretion (33) and solar tides from (35) using $k_{2m}MR_e^2/C_m = 0.5$. The angular orientation corresponds to $\ell = 0°$.

Figure 9. Comparison of observed and model semiannual amplitude in rotation angle, $\delta\phi$.

Figure 10. Triannual model contributions.

Figure 11. Shown are the factors which affect the tidal ($k_{2m}MR_e^2/C_m$) and ice cap (($1 + k'_{2m})MR_e^2/C_m$.) contribution to rotation, respectively. Also, $k'_{2m} \simeq -k_{2m}$.

Figure 12. Wobble and FCN nutation frequencies versus moment C for 3 hot models.

Figure 13. Predicted forced polar motion amplitude based on the uniform cap model and $\simeq 1.5°$ offset.

Figure 14. The core F factor for three hot mantle profile models.

Figure 15. Nonrigid response for five frequencies (see (47) and Table 5). In Figures 15a and 15c, the annual and semiannual prograde amplitudes are shown, respectively. In the remaining panels, the amplitudes for the retrograde annual, semiannual, and triannual lines are displayed.

Figure 16. Predicted amplitudes for seasonal variations in normalized zonal harmonics J_n for $n = 2, 3, 4$ and 5. The estimates assume uniform accretion/sublimation and cap angular radius of $35°$. The sensitivity (a factor of 10 smaller than that claimed by *Chao and Rubincam* [1990]) is based on standard deviations for Venus gravity [*Konopliv and Sjogren*, 1996] which have been multiplied by a factor of 2.4 to account for the different mass and radius of Mars.
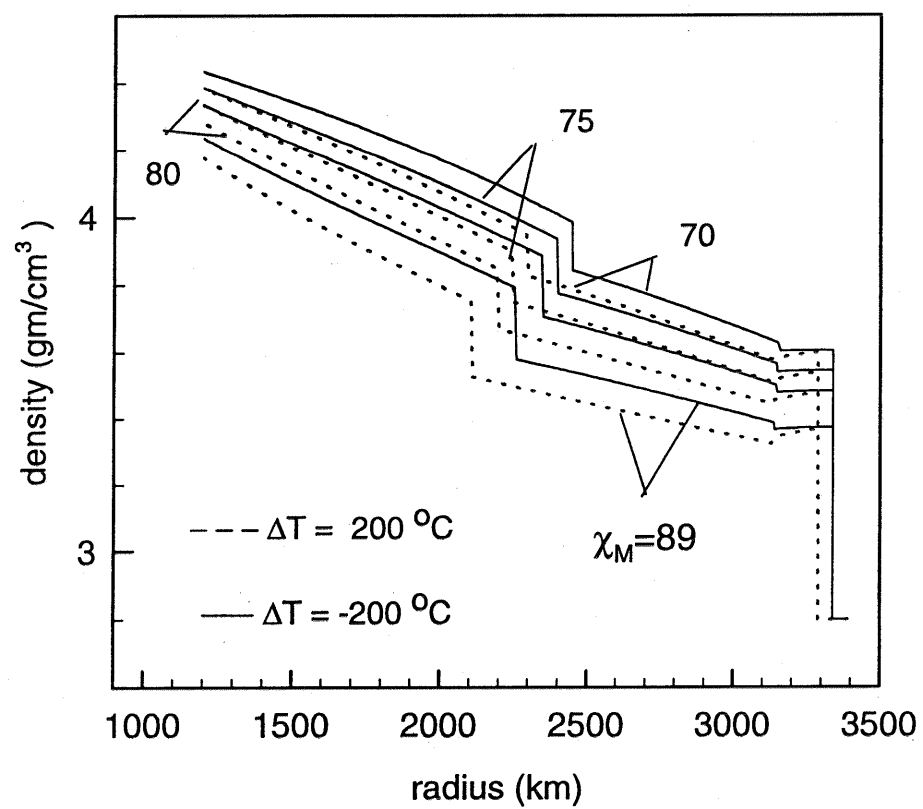
Figure 1
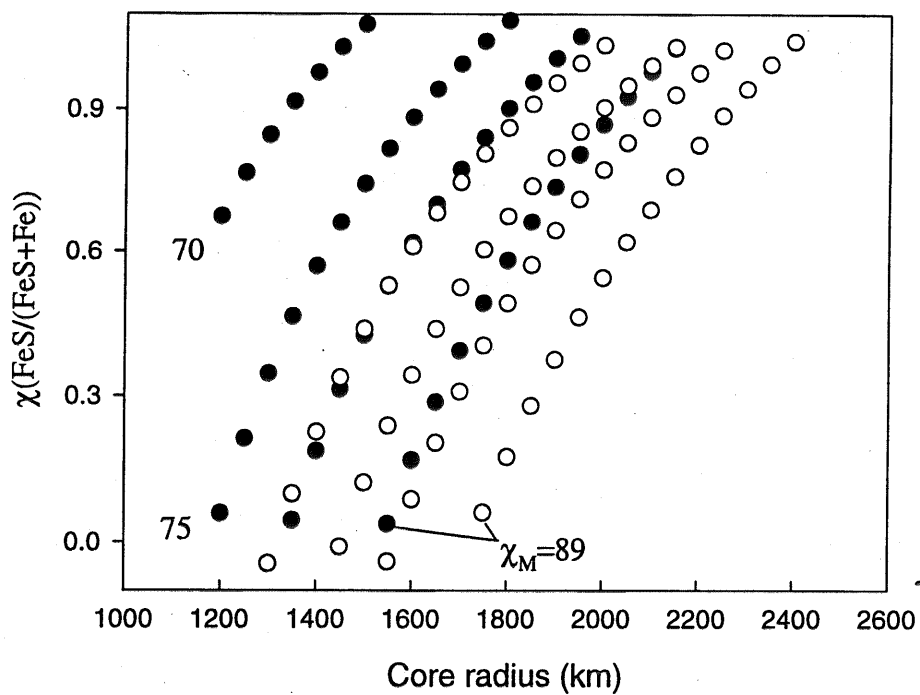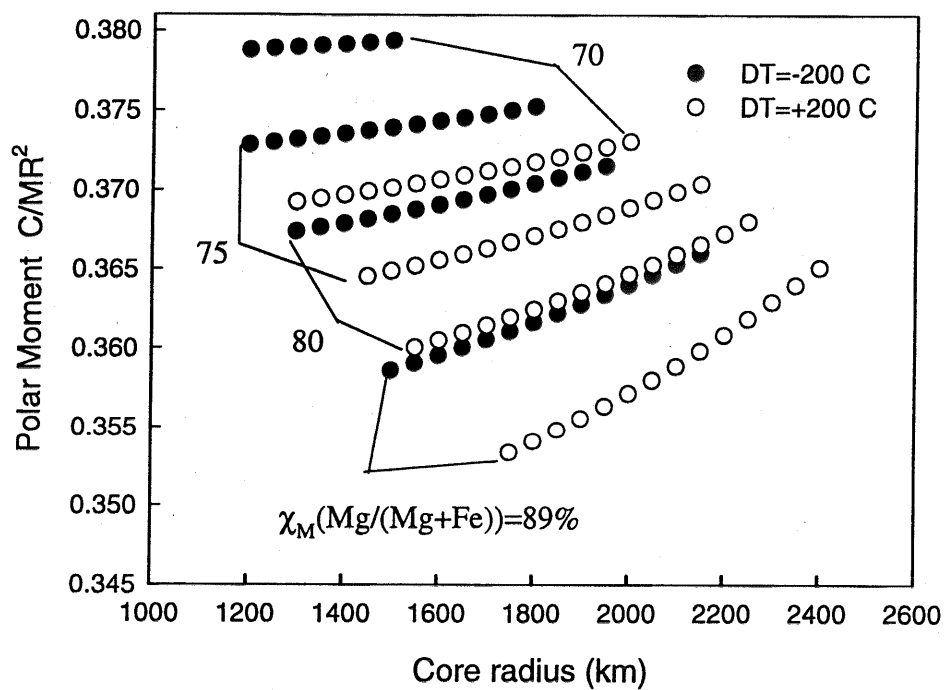
Figure 2
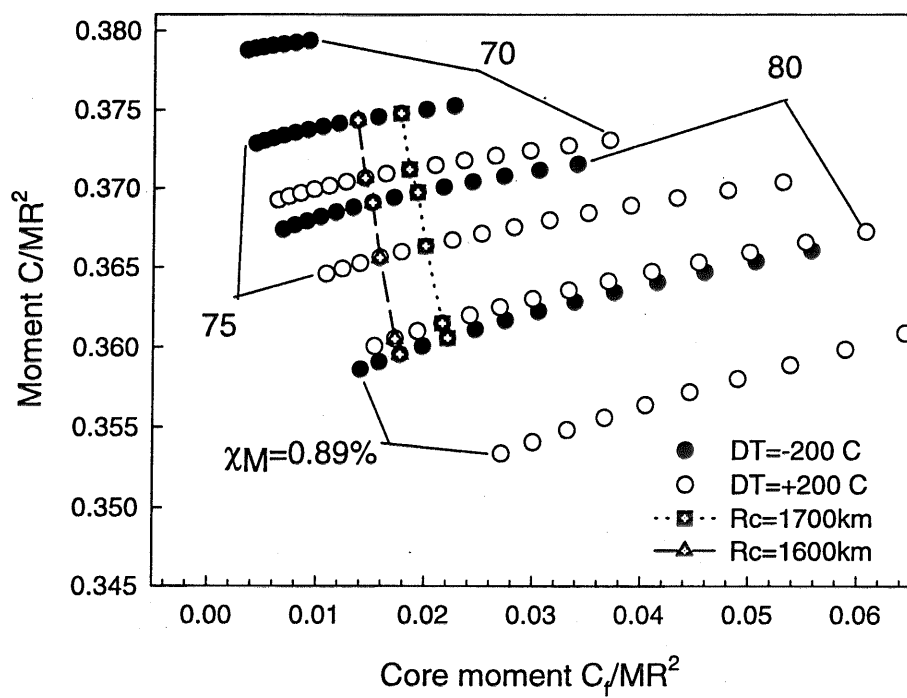
Figure 3
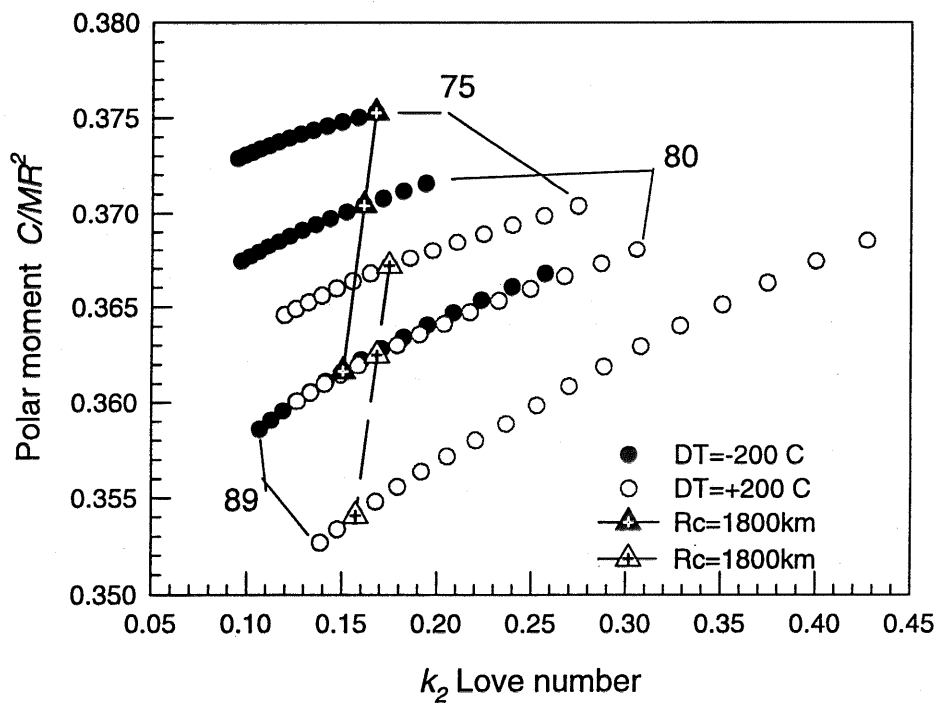
Figure 4
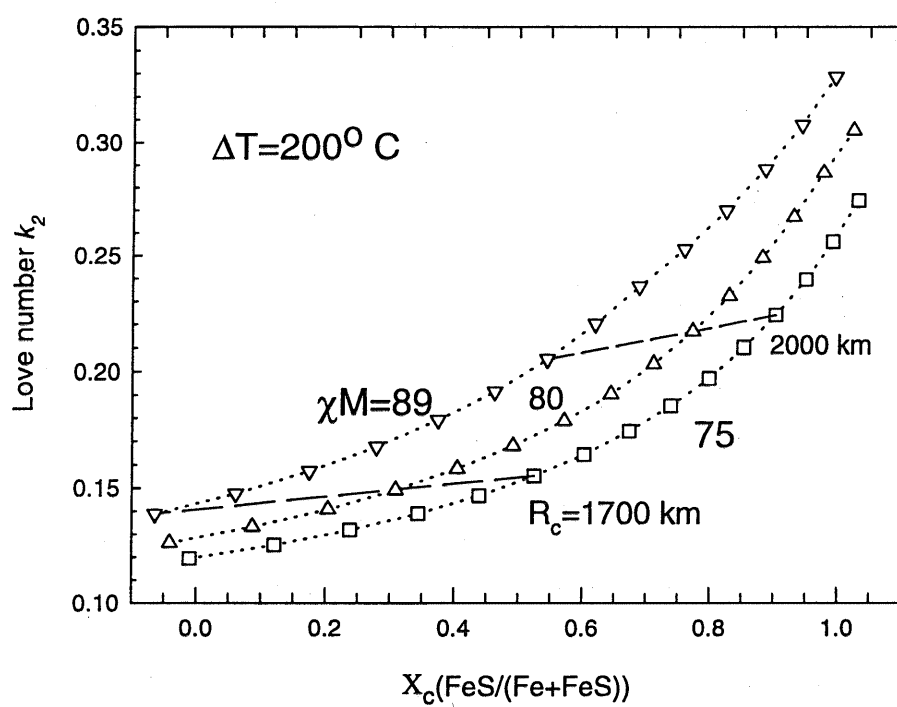
Figure 5
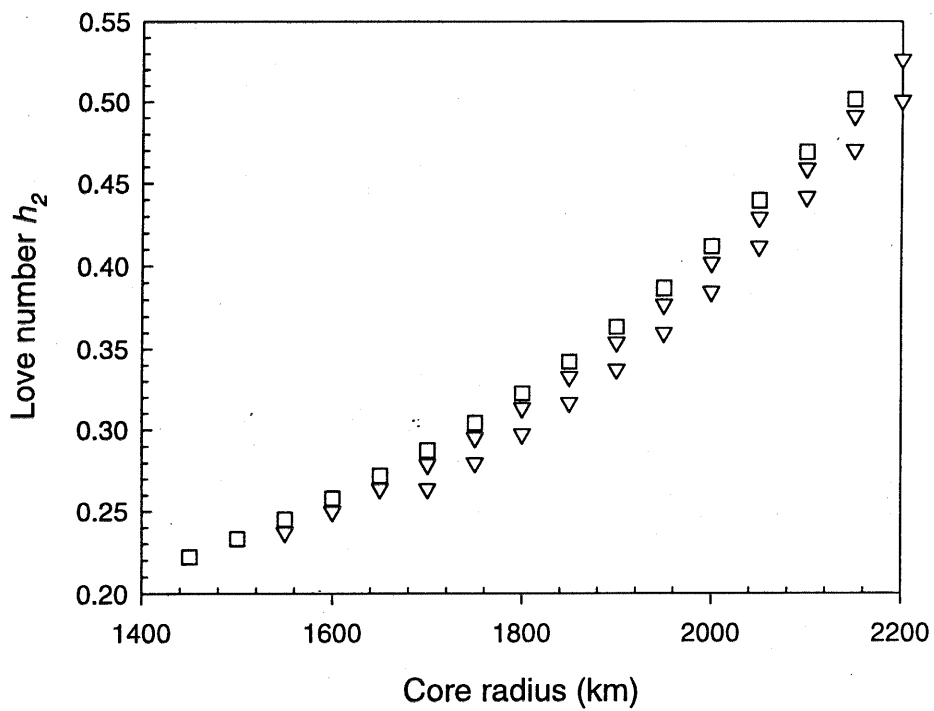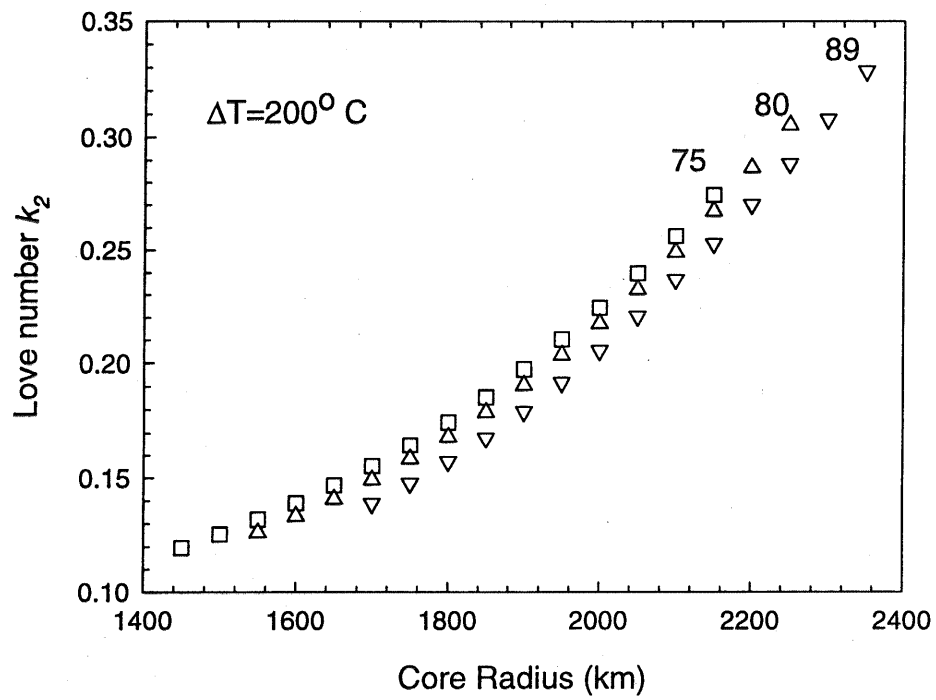
Figure 6
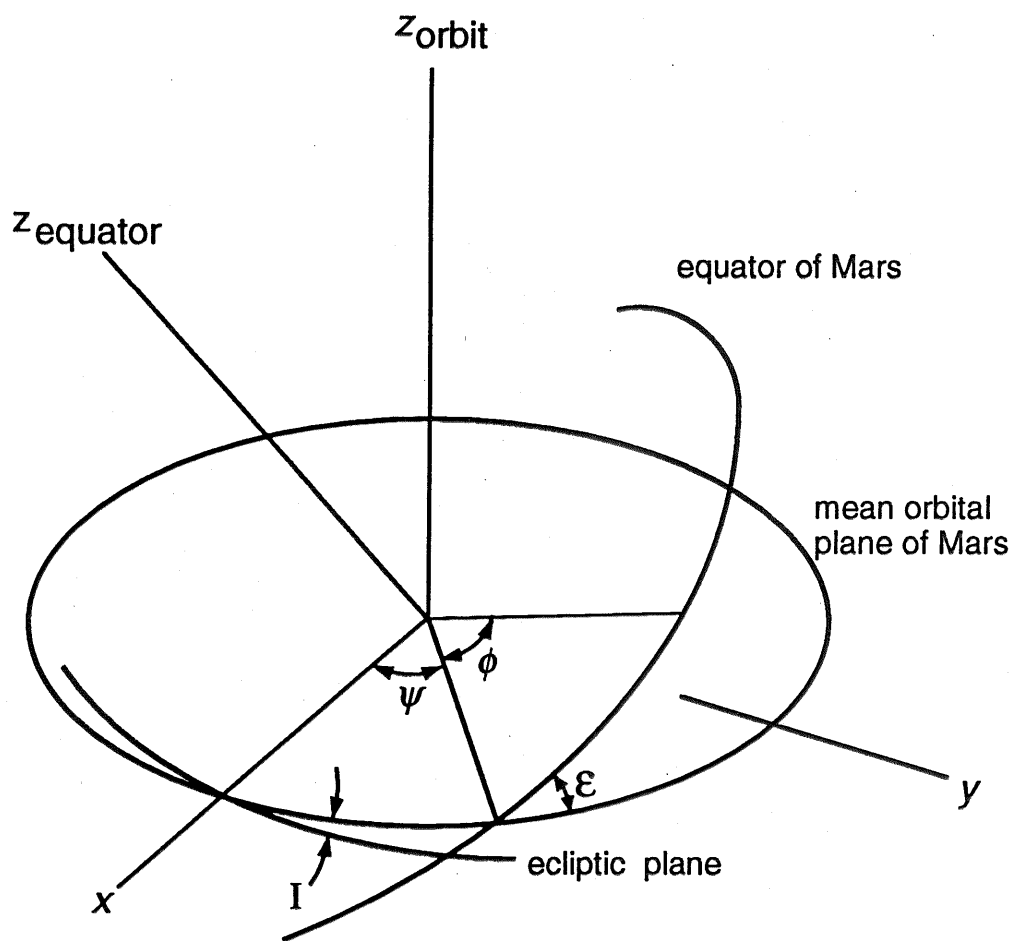
Figure 7

Rotation angle: δφ
Annual term
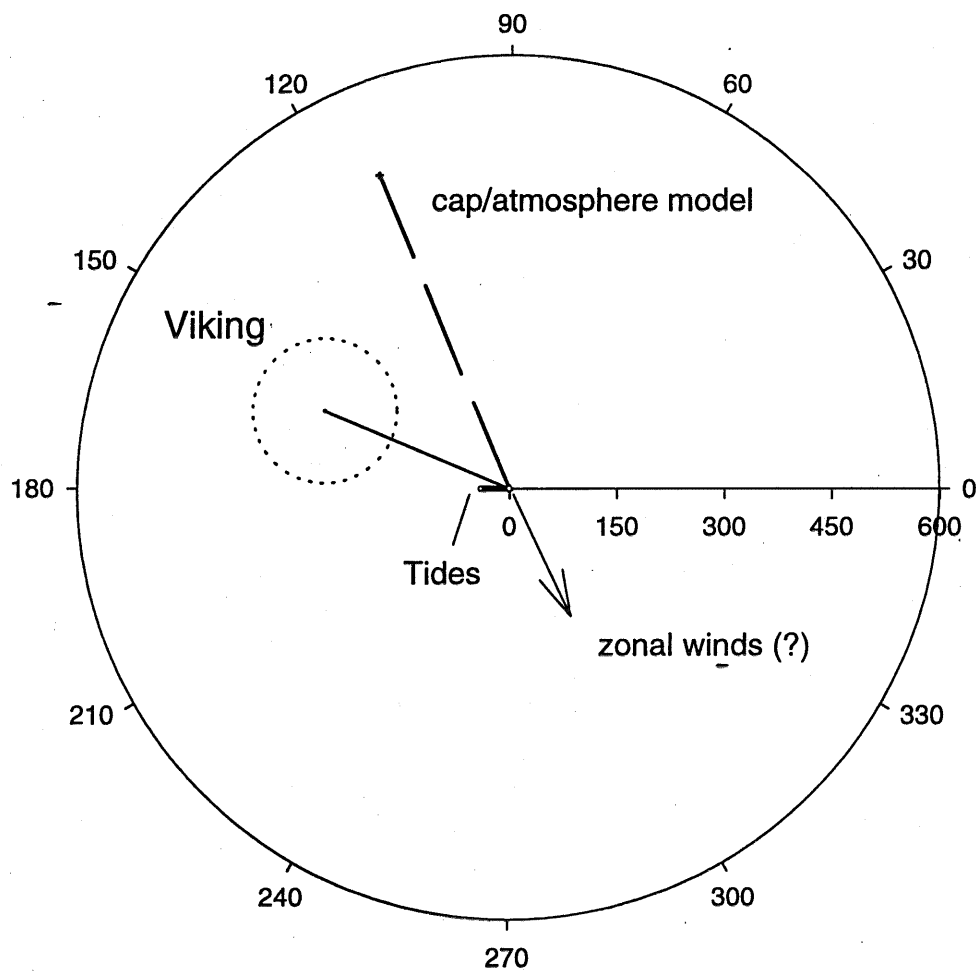
Figure 8

Rotation angle: δφ
Semiannual term
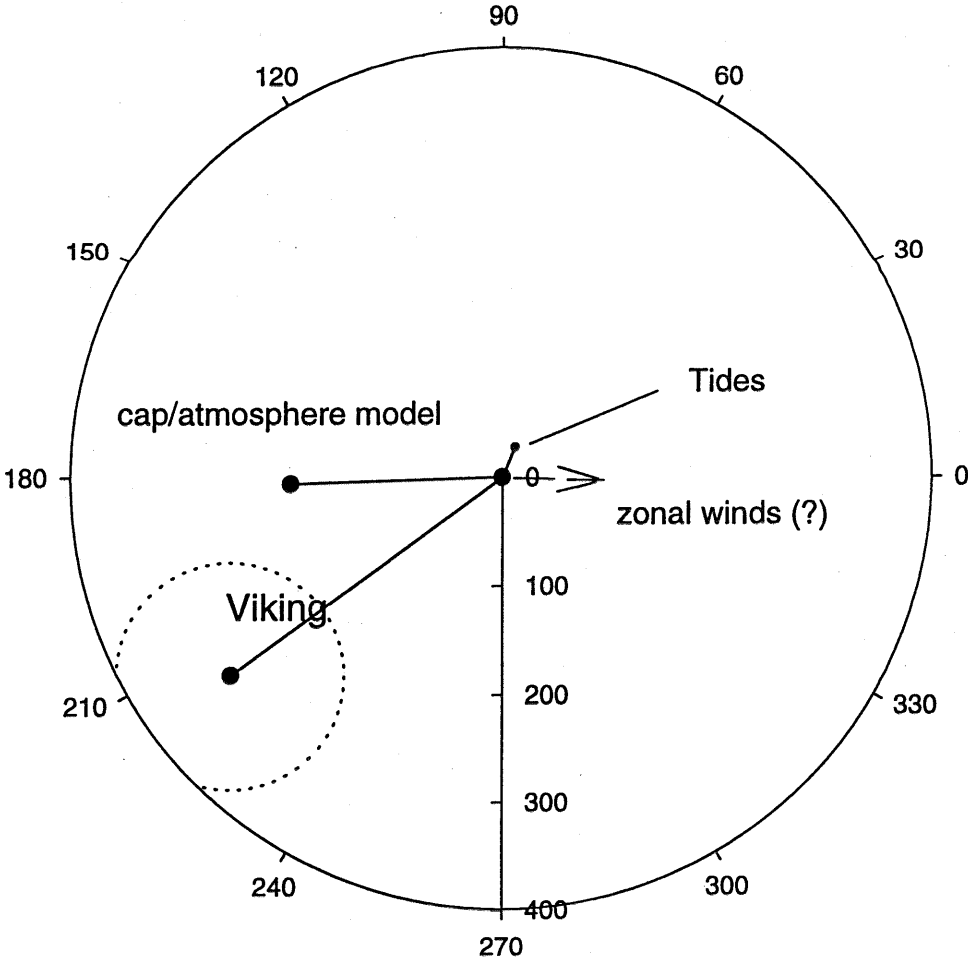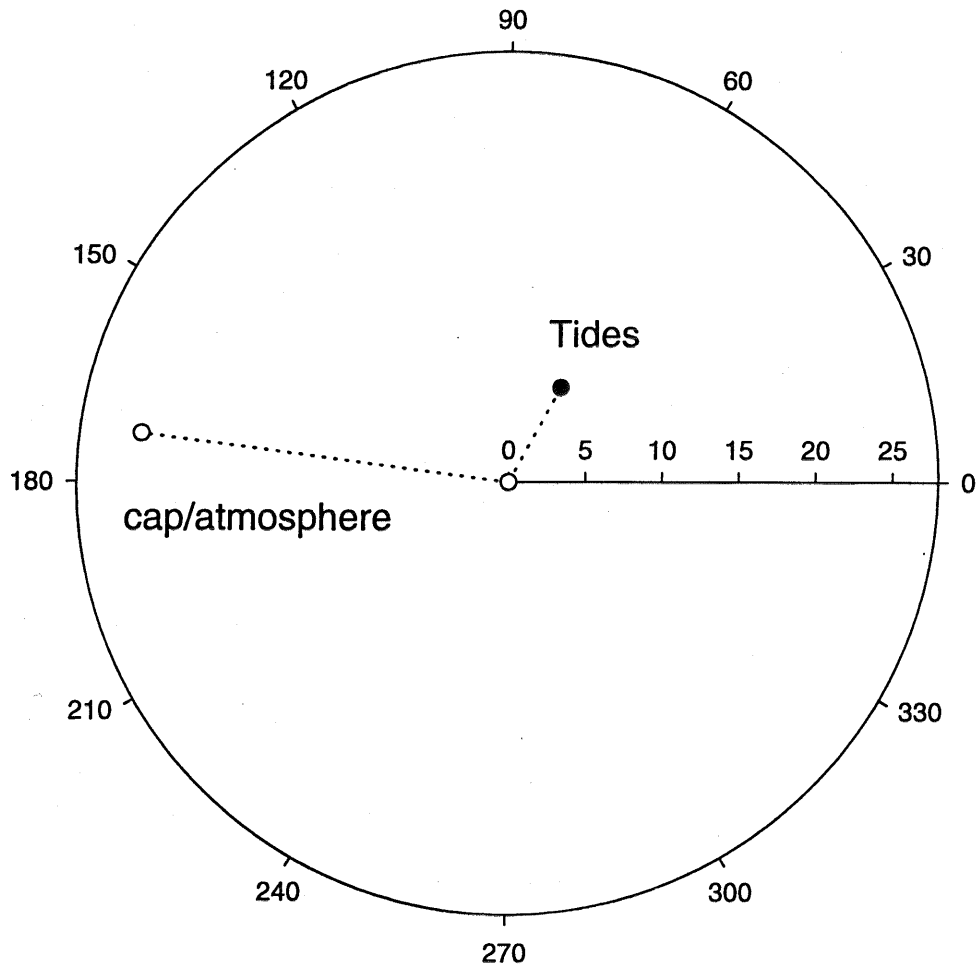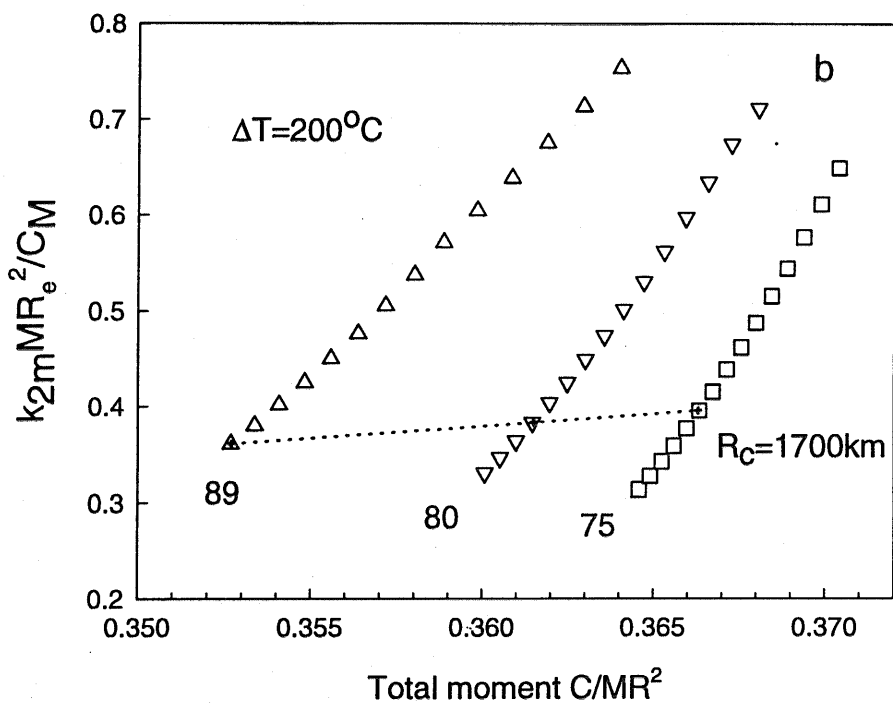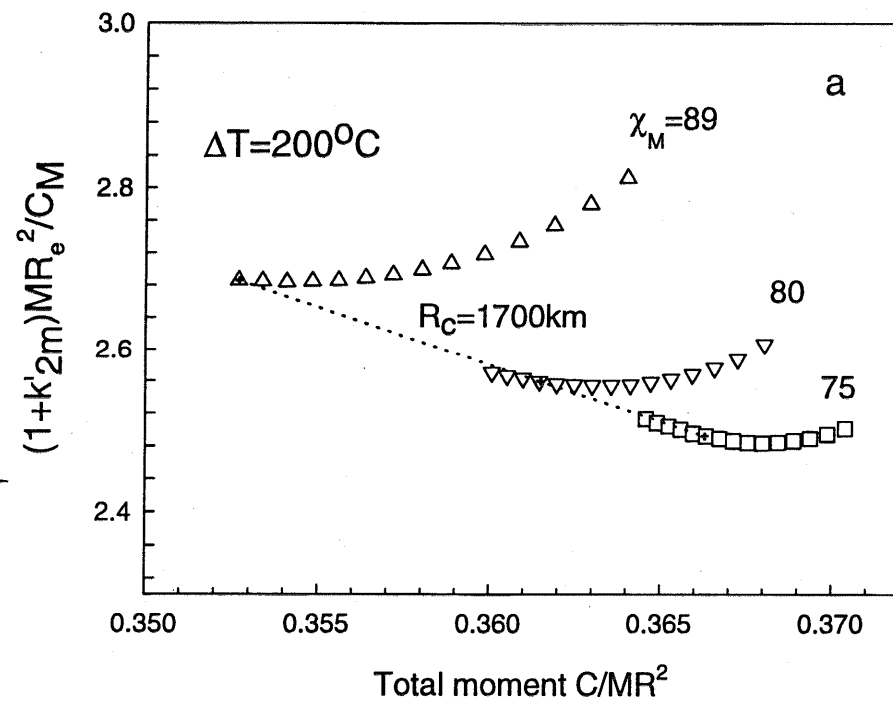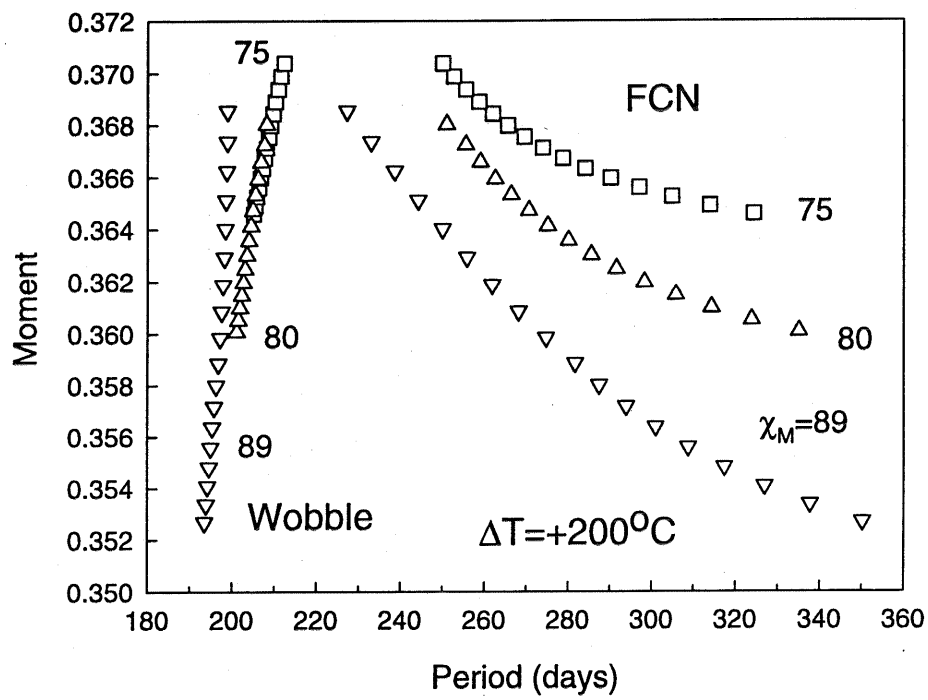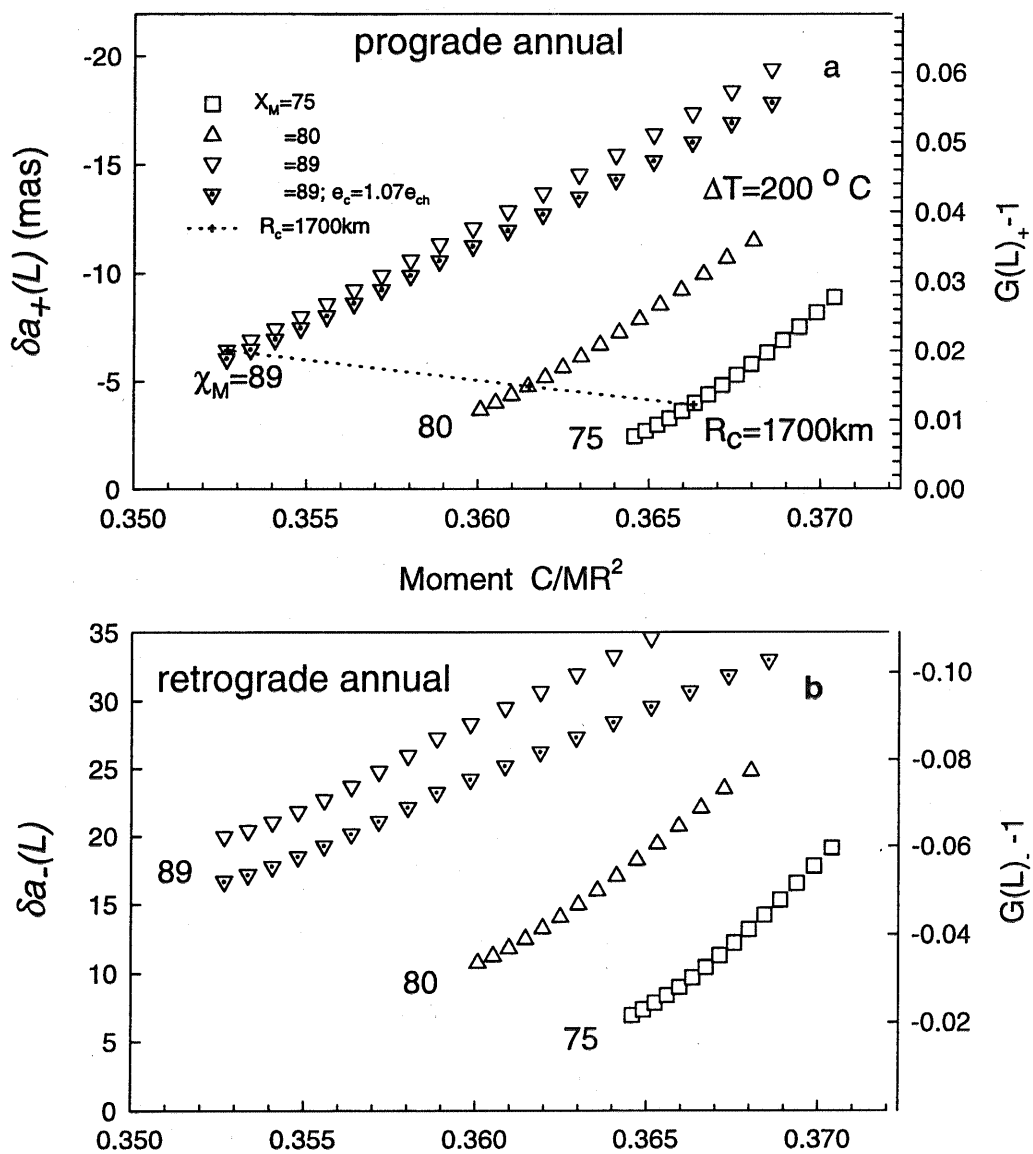

Figure 9

Triannual model for δφ
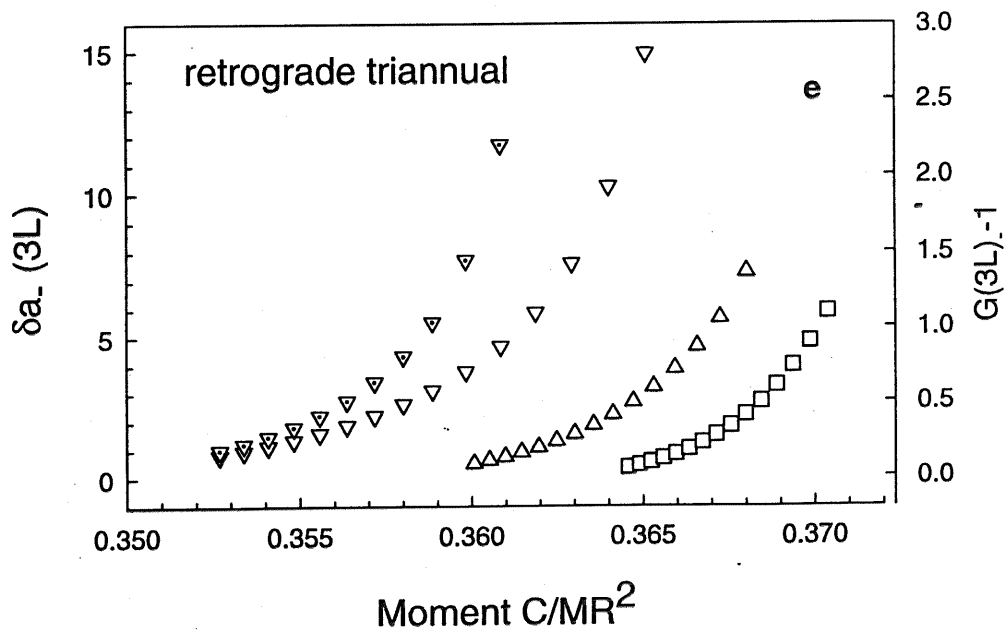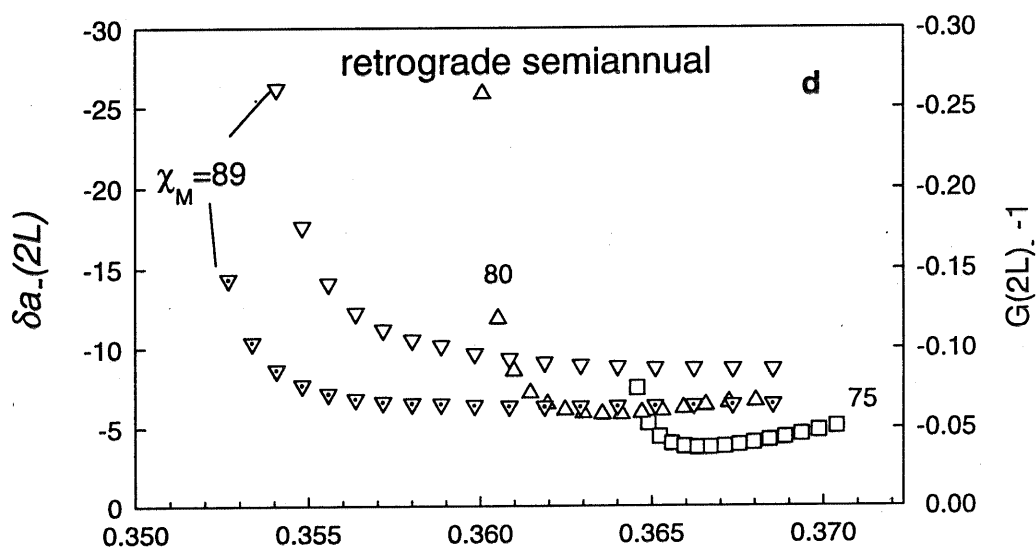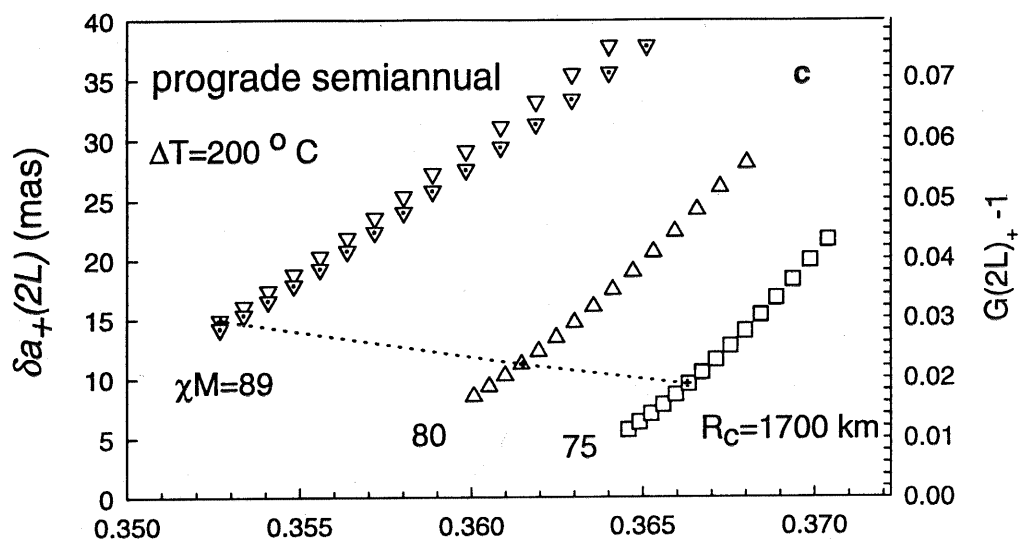

Figure 10

Figure 11

Figure 12
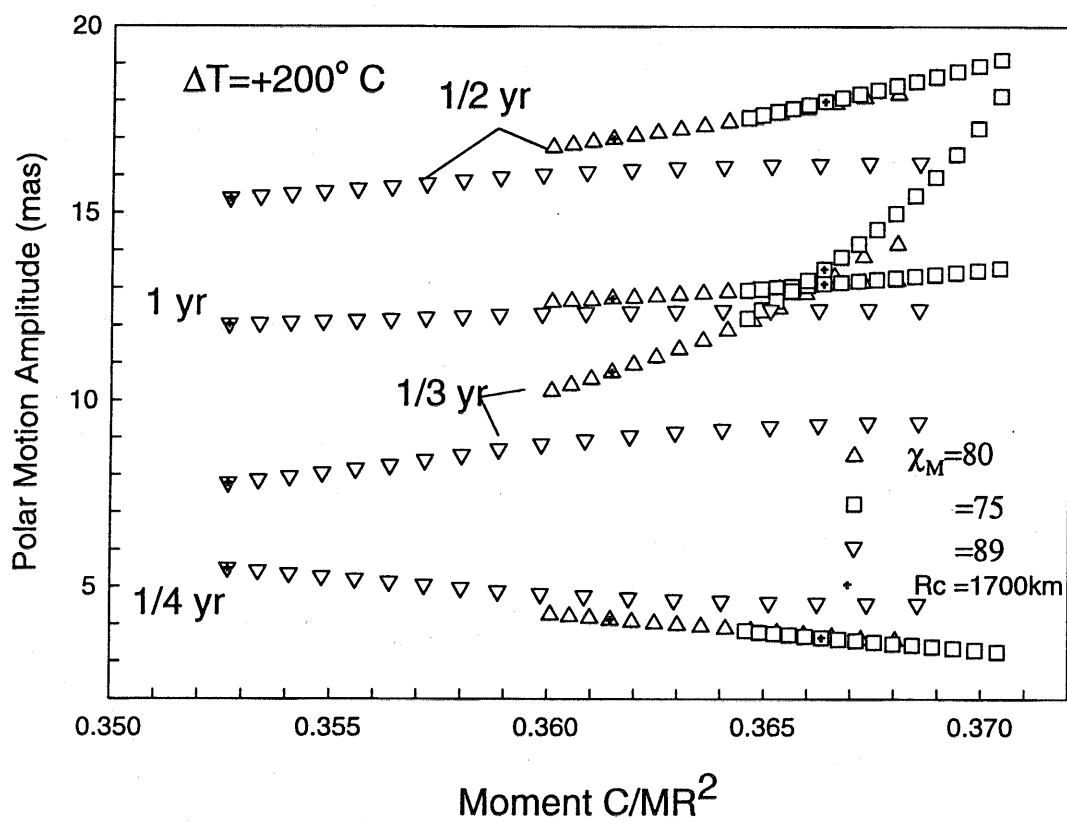
Figure 13
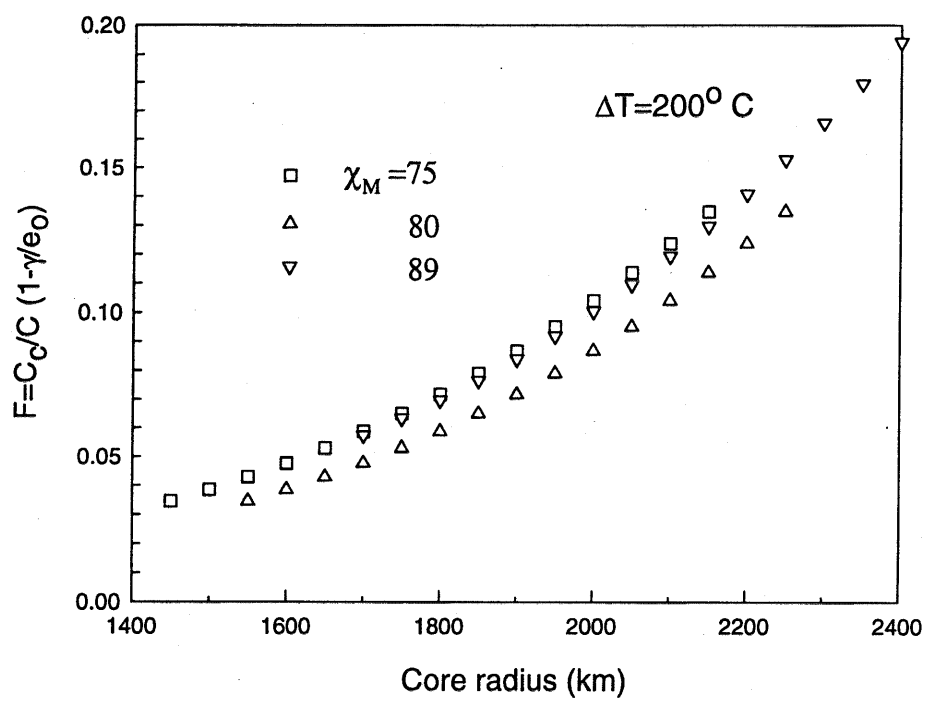
Figure 14

Figure 15 a, b

Figure 15, c, d, e

Figure 16